Cenozoic exhumation and deformation of northeastern Tibet and the Qinling: Is Tibetan lower crustal flow diverging around the Sichuan Basin?

Eva Enkelmann[†]
Lothar Ratschbacher
Raymond Jonckheere
Ralf Nestler
Manja Fleischer
Richard Gloaguen
Geowissenschaften, Technische Universität Bergakademie, D-09599 Freiberg, Germany

Bradley R. Hacker
Geological Sciences, University of California, Santa Barbara, California 93160, USA

Yue Qiao Zhang
Yin-Sheng Ma
Institute of Geomechanics, Chinese Academy of Geological Sciences, Beijing 100081, People's Republic of China

ABSTRACT

Apatite fission-track thermochronology data elucidate the cooling/exhumation history of the Qinling (Qin Mountains), which contain a Paleozoic–Mesozoic orogenic collage north of the Sichuan Basin and northeast of the Tibetan Plateau. In particular, we examine the extent to which the Qinling were affected by the rising plateau. The northern and eastern Qinling show continuous cooling and slow exhumation since the Cretaceous. In contrast, in the southwestern Qinling, rapid cooling initiated at 9–4 Ma, a few million years later than in the eastern Tibetan Plateau. A compilation of major Cenozoic faults in the eastern Tibetan Plateau and the Qinling, and their kinematic and dynamic characterization, shows that deformation in the Qinling has predominantly been strike slip. Active sinistral and dextral strike-slip faults delineate an area of eastward rock flow and bound the area of rapid late Cenozoic cooling outlined by apatite fission-track thermochronology. These data can be interpreted to indicate that lower crustal flow has been diverted around the Longmen Shan and beneath the southwestern Qinling, causing active plateau uplift in this area. Alternatively, northeastern Tibet may be growing eastward faster in the western Qinling than the entire South China Block is extruding to the east.

Keywords: Tibet, Qinling, plateau growth, fission track, structural geology.

INTRODUCTION

The Tibetan Plateau displays doubled crustal thickness (~60–70 km in central Tibet; Zhao et al., 2001) and topography elevated to 4–5 km (Fielding et al., 1994). Whereas crustal thickening and plateau uplift north of the Indian indenter are mainly attributed to shortening (Tapponnier et al., 2001; here called the plateau growth–backstop model), it has been proposed that thickening east of the eastern Himalayan syntaxis, i.e., in eastern Tibet, is mostly the result of lower crustal flow (Royden et al., 1997; Clark and Royden, 2000; here called the lower crustal flow model). The first model suggests growth of the eastern part of the plateau by oblique thrusting and folding, delineated by major strike-slip faults such as the Altyn Tagh and Haiyuan faults (Fig. 1A) and backstops, as the North and South China Cratons and the Tarim Block (Fig. 1A). In the second model, lower crust of the central plateau has flowed eastward over distances of >1000 km. This has created gently sloping topography and a broad, gentle plateau margin where the lower crust beneath the margin and adjacent foreland is weak, and steep topography where lower crustal flow is inhibited by a strong margin. In the eastern Tibetan Plateau, the strong South China Craton beneath the Sichuan Basin (Fig. 1B) was suggested to have caused the flow to "pile up" and create a narrow, steep margin; diversion of the flow to the north into northeastern Tibet and the Qinling (Fig. 1B) and south into southeastern Tibet created broad, gentle margins and active plateau growth.

Irrespective of which model applies, geologic and geodetic data showcase northeast- and east-directed shortening and related uplift of the northeastern Tibetan Plateau. Cumulative regional shortening appears to be ≤15 mm/yr over the last 10 m.y. (Tapponnier et al., 2001), and geodetic results imply similar or slower rates of dextral motion between the northeastern plateau (i.e., the area north of the Kunlun fault) and the Sichuan Basin (Chen et al., 2000; Zhang et al., 2004). Whereas the deformation front along the plateau margin is clearly defined in the north by the sinistral strike-slip Altyn Tagh and Haiyuan faults and associated transpressional fold-thrust belts (Fig. 2A; e.g., Meyer et al., 1998), its south(eastern) margin north(west) of the Sichuan Basin is poorly defined, and dextral strike-slip faults have yet to be found within the Longmen Shan and the western Qinling (Burchfiel et al., 1995). The higher rates of shortening in the northeastern Tibetan Plateau in comparison to the margins of the Sichuan Basin imply

[†]Present address: Earth and Environmental Sciences, Lehigh University, Bethlehem, Pennsylvania 18015, USA; e-mail: eva.enkelmann@lehigh.edu.

GSA Bulletin; May/June 2006; v. 118; no. 5/6; p. 651–671; doi: 10.1130/B25805.1; 9 figures; 4 tables.

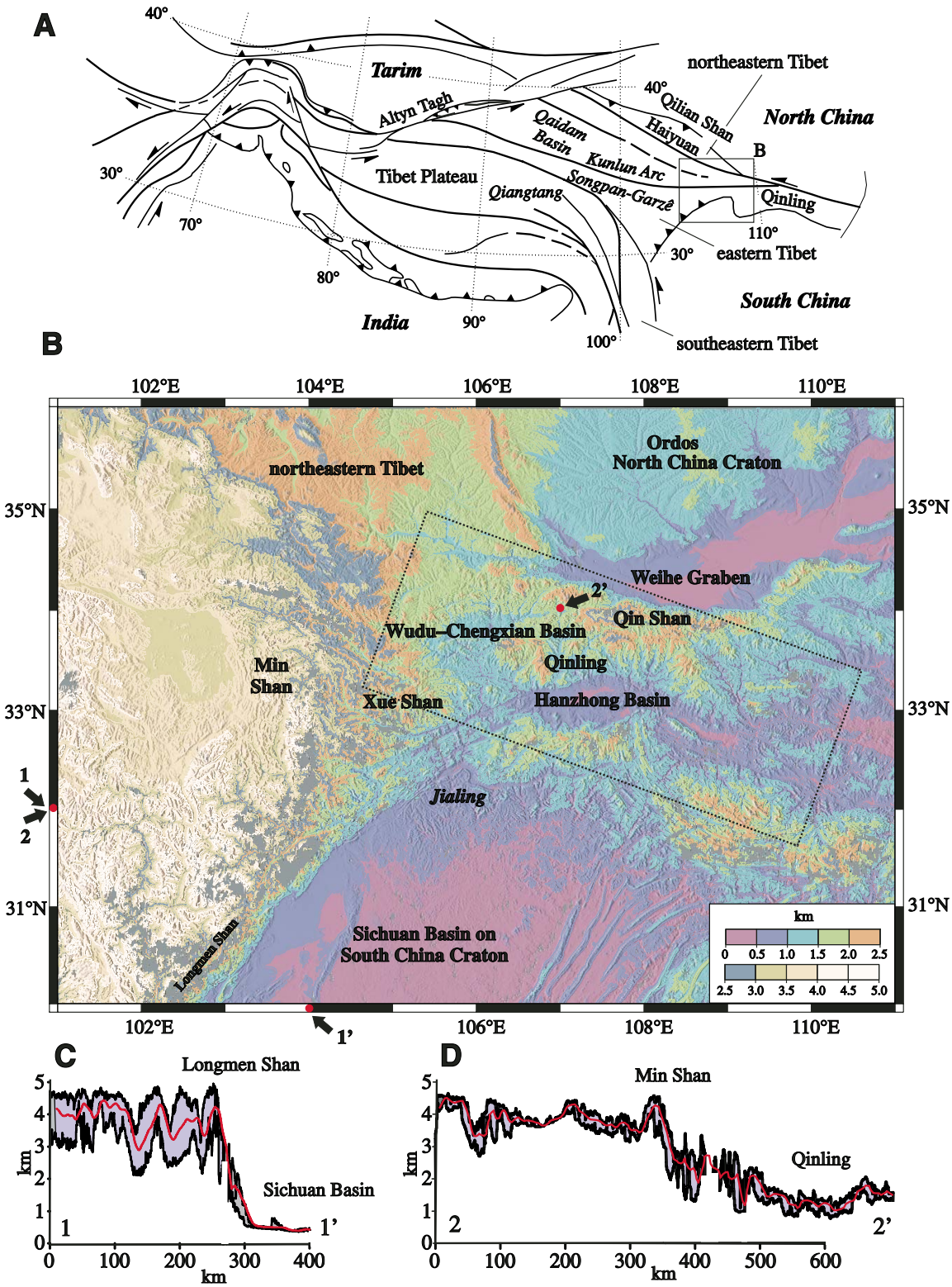

Figure 1. (A) Regional tectonic map of the Pamirs and Tibet, showing major suture zones (thick lines), Cenozoic fault systems, backstops (India, Tarim, North and South China Cratons; in bold italics), faults (Altyn Tagh, Haiyuan), and lithotectonic (in italics) and geographic units used in text. Modified from Schwab et al. (2004). Rectangle outlines Figure 1B. (B) Topographic map and (C) and (D) topographic swath profiles across northeastern Tibet and the western Qinling. The topographic data stem from the SRTM digital elevation model data set with 90 m horizontal resolution. The 20-km-wide swaths extract a rectangular patch of topography, and its values are projected onto a vertical plane parallel to the long axis of the swath; maximum, mean (red), and minimum topographic curves are shown. Jialing: river draining the Min and Xue Shan. Rectangle outlines area displayed in Figures 2 and 3.

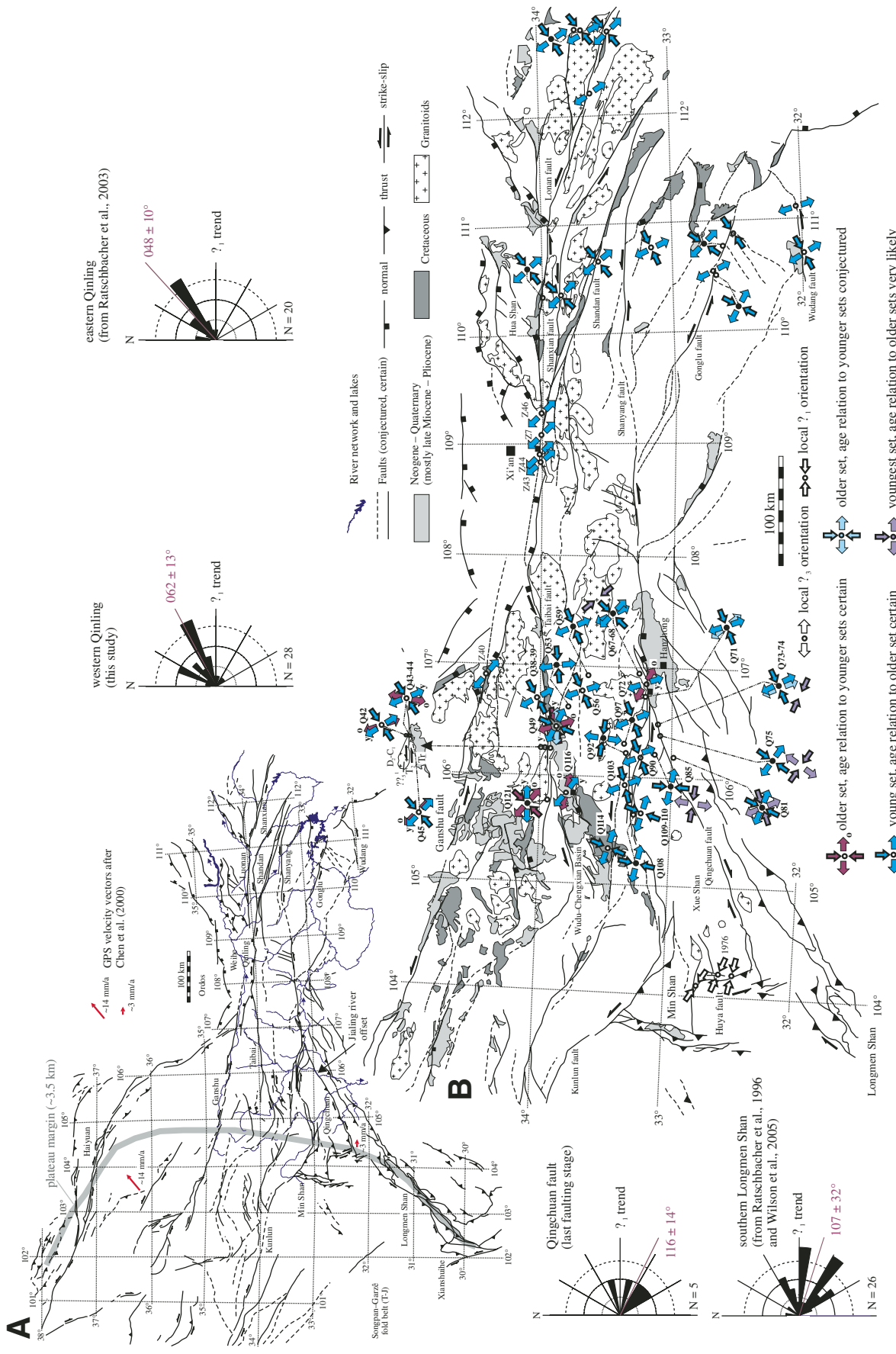

Figure 2. (A) Compilation of likely Cenozoic faults in northeastern Tibet and the Qinling, based on Chinese maps, published studies, and our field work (see text for references). Red arrows give GPS velocity vectors in Eurasian reference frame, likely describing active growth of the northeastern Tibetan Plateau and the Longmen Shan (Chen et al., 2000) and the distributed dextral strike-slip deformation between northeastern Tibet and the Sichuan Basin. (B) Major faults, Cretaceous–Holocene sedimentary basins within the Qinling, and regional deformation field characterized by mesoscale fault-slip data. The regional stress-axis distribution likely encompasses the Neogene–Holocene; the differently aged sets within this "neotectonic" stress field are based on relative overprinting criteria determined in the field. All data from this study except for Huya data are from focal-mechanism solutions of Jones et al. (1984), "Z" stations along Weihe graben from Zhang et al. (1998), and eastern Qinling from Ratschbacher et al. (2003). Rose diagrams compile σ_1 orientations from subregions discussed separately in the text.

clockwise rotation of crust at the eastern edge of the plateau.

Both the lower crustal flow and the plateau growth–backstop models predict eastward diminishing late Cenozoic to Holocene surface uplift, exhumation, and deformation in the Qinling. Here, we use apatite fission-track thermochronology to elucidate the cooling-exhumation history of the Qinling; in particular, we focus on the extent to which the Qinling were affected by the rising Tibetan Plateau. We show that continuous cooling and slow exhumation recorded in the northern and eastern Qinling contrast with rapid cooling at the end of the thermal history in the southwestern Qinling. We also compile data related to major Cenozoic structures of the western Qinling and characterize them kinematically and dynamically: sinistral and dextral strike-slip boundaries, active at the end of deformation history, bound the area of rapid late Cenozoic cooling outlined by apatite fission-track thermochronology, delineating an area of eastward rock flow. Our study may indicate that, following its diversion around the Longmen Shan, lower crustal flow may be causing active plateau uplift in the southwestern Qinling. Alternatively, the western Qinling may be growing eastward faster than the entire South China Craton is extruding to the east.

GEOLOGICAL SETTING

The eastern Tibetan Plateau is composed of the Songpan-Garzê fold-thrust belt and the Longmen Shan fold-thrust belt, which are bounded to the north and northeast by the Paleozoic–Mesozoic East Kunlun Arc and Qinling orogen, and to the southeast and southwest by the South China Craton and the Qiangtang Block of central Tibet (Fig. 1A, B). The Songpan-Garzê belt contains 5–15 km of flysch deposited mainly in the Triassic; it was tightly folded during the Late Triassic–Early Jurassic Indosinian orogeny (Mattauer et al., 1992; Nie et al., 1994; Harrowfield and Wilson, 2005). The Longmen Shan thrust belt separates the Songpan-Garzê belt from the Sichuan Basin (on the South China Craton; Chen et al., 1995; Chen and Wilson, 1996) and is characterized by east-southeast–directed thrusts initiated during the Late Triassic (Dirks et al., 1994; Burchfiel et al., 1995). The Cenozoic India-Asia collision imprinted conjugate, roughly west-northwest–striking sinistral and north-northwest–striking dextral, strike-slip fault zones onto eastern Tibetan crust (Tapponnier and Molnar, 1977; Wang and Burchfiel, 2000), and reactivated the Longmen Shan thrust belt (Dirks et al., 1994; Burchfiel et al., 1995; Fig. 2A).

The Longmen Shan are a major topographic feature with elevations between ~0.6 km (southern Sichuan Basin) and ~6.5 km over a horizontal distance of ~50 km (Fig. 1B, C). The north-trending Min Shan (Figs. 1B, 2B), located between the Kunlun fault zone and the Longmen Shan, define the topographic front of the east-northeastern plateau; mean elevation drops from ~4.0 km on the plateau to ~1.2 km in the southwestern Qinling (Fig. 1B, 1D). Despite the high topography, the lack of a pronounced foredeep in the Sichuan Basin indicates that Cenozoic shortening across the Longmen Shan plateau margin was minor (Burchfiel et al., 1995; Royden et al., 1997); geodetic studies record 2–6 mm/yr shortening across the Longmen Shan (King et al., 1997; Chen et al., 2000; Zhang et al., 2004). The initiation of deformation between the Longmen Shan and the Qilian Shan, which marks the Cenozoic deformation front in the north-northeastern part of the plateau, is probably not older than ca. 5 Ma on the basis of the timing of deformation in the northern Qaidam Basin and the Qilian Shan (Fig. 1A; Metivier et al., 1998; Meyer et al., 1998).

The east-trending Qinling separate the North China and the South China Cratons (Fig. 1A, B) over >1000 km. The mountain range is composed of different units assembled during the late Proterozoic–early Mesozoic and sliced by east-striking fault zones whose orientation and deformation suggest several hundreds of kilometers of ductile displacement during the Paleozoic–early Mesozoic, overprinted by Late Cretaceous and Cenozoic brittle deformation (Mattauer et al., 1985; Peltzer et al., 1985; Ratschbacher et al., 2003). Active faulting in the Qinling is interpreted as the eastward continuation of the Haiyuan, Ganzu, and Kunlun sinistral strike-slip fault zones (Fig. 2A; Zhang et al., 1995) and the southern termination of extensional tectonics in the North China Craton that fragmented the Precambrian craton into horsts and grabens around the Ordos Block (Zhang et al., 1998). Peltzer et al. (1985) and Zhang et al. (1995) suggested cumulative active sinistral strike-slip rates of ~7 mm/yr for the northern Qinling faults south of the Weihe graben (Fig. 1B), and Ratschbacher et al. (2003) highlighted the widespread Cenozoic reactivation of the eastern Qinling.

Previous low-temperature thermochronologic studies that addressed the exhumation of eastern Tibet focused on the sinistral Xianshuihe strike-slip fault zone in the Songpan-Garzê fold belt (Xu and Kamp, 2000), the topographic front along the eastern margin of the plateau (Longmen Shan; Arne et al., 1997; Kirby et al., 2002), and southeastern Tibet (Clark et al., 2005; Figs. 1A, 1B, 2). Along the topographic front, increased cooling (30–50 °C/m.y.) has been active since the late Miocene or early Pliocene (5–12 Ma), and exhumation has amounted to 8–10 km; Kirby et al. (2002) concluded that if lower crustal flow had occurred, it did not reach the Longmen Shan before this time. $^{40}Ar/^{39}Ar$ K-feldspar and (U-Th)/He zircon and apatite thermochronology data also indicate that cooling in the interior of the Songpan-Garzê belt was slow (~3 °C/m.y.), with 1–2 km of exhumation from the Jurassic to the late Miocene or early Pliocene. A slight increase in cooling rates in the middle Tertiary, however, might reflect a migrating wedge of gently sloping topography, which can be interpreted as an expression of lower crustal flow (Kirby et al., 2002). In southeastern Tibet, apatite fission-track and (U-Th)/He thermochronology data suggest that a change from slow to rapid cooling occurred after ca. 13 Ma (Clark et al., 2005). Using age versus elevation relationships of apatite fission-track and (U-Th)/He data from fault-bounded blocks of the interior (Songpan-Garzê fold belt) and the eastern margin (Longmen Shan) of the eastern Tibetan Plateau, Enkelmann et al. (2004) showed that an extensive period of tectonic quiescence was terminated at 16–10 Ma by rapid exhumation. The thermochronologic studies are in line with geomorphologic analyses: Schoenbohm et al. (2004) used a reconstruction of river incision into a regional low-relief "relict" landscape preserved over the eastern margin of the Tibetan Plateau to propose that growth of the plateau margin in southeastern Tibet began in the Pliocene after uplift of the plateau adjacent to the Sichuan Basin in the middle Miocene to early Pliocene. Similarly, Kirby et al. (2003) and Clark et al. (2004) used local and regional analyses of the drainage evolution of eastern Tibet to demonstrate that the development of the drainage patterns is related to the Miocene(?)–Holocene uplift of the plateau margin.

APATITE FISSION-TRACK DATA

Forty-eight samples from the Qinling were selected for apatite fission-track analysis. For most samples from the eastern Qinling, the geological background, petrology, and high-temperature thermal evolution are reported in Ratschbacher et al. (2003). Appendix 1 details the technical and methodological aspects—i.e., sample preparation, irradiation, age calculation, measurements of kinetic parameters, and our approach to thermal history (T[t]-path) modeling. Figure 3 and Table 1 specify sample location, lithology, and regional age distribution. We calculated the fission-track ages with the standard based Z and ζ methods and the independent (absolute) ϕ method (Jonckheere, 2003a); the ages are summarized in Table 1, and, within

1σ, the ages obtained from the three different methods agree (Fig. A1). In the following, we use ϕ ages. Table 2 lists the track-length data.

Most Qinling samples have Late Cretaceous to Eocene apatite fission-track ages (Table 1). There are no obvious regional age clusters and no age-elevation correlations (Fig. 3; Table 1). However, the fission-track age versus the mean track length correlation (Fig. 4A) reveals an incomplete boomerang (Green, 1986), defined by samples with apparent fission-track ages of ca. 40–60 Ma and mean track lengths <12 μm, which contrast with samples with ages of ca. 50–150 Ma and mean track lengths >12 μm; this suggests the presence of distinct cooling histories within the study area. To identify these distinct cooling histories preserved in the track-length distributions, we plotted the samples in a diagram relating mean track lengths, standard deviations, and skewness (Fig. 4B). Three groups can be differentiated: group 1 shows mean track lengths ≥13 μm, small standard deviations, and low skewness; group 2 has negative skewness and both shorter mean track lengths and higher standard deviations than group 1; group 3 displays short mean track lengths (≤12.2 μm), high standard deviations, but low skewness.

The three length-distribution groups represent distinct thermal (cooling) histories. Figure 5 displays track-length distributions for all samples with more than 30 confined tracks, and presents T[t]-path modeling results (using AFTSolve 1.1.3; Ketcham et al., 2000) of eight samples with a large number of confined tracks, to illustrate the three distinct cooling-history groups. Cooling group 1 (samples Q1, Q43, Q44, Q122, Q123, Q124, Q127) indicates rapid cooling to low temperatures followed by prolonged time at these temperatures. Cooling group 2 (Q3, Q31, Q32, Q37, Q76, D415, D427, D436, HC128, HC130), with the negatively skewed distribution, indicates continuous cooling through the ~100 °C isotherm to surface temperatures since the time given by the apparent fission-track ages. Cooling group 3 (Q4, Q8, Q55, Q65, Q67, Q69, Q113, DS430), with the symmetric track-length distributions, indicates a long residence time within the upper (low-temperature) part of the partial annealing zone (PAZ; ~60–90 °C), followed by rapid cooling at the end of the thermal history.

The three cooling-history groups show a distinct regional distribution, implying regional variation in time and/or amount of cooling (Fig. 3). Group 1 samples occur along the Ganshu fault (Q122, Q123, Q124, Q127), the northern margin of the western Qinling, and along the Taibai fault (Q43, Q44) that forms the northern boundary of the Cretaceous–Tertiary Wudu-Chengxian Basin. Apatite fission-track

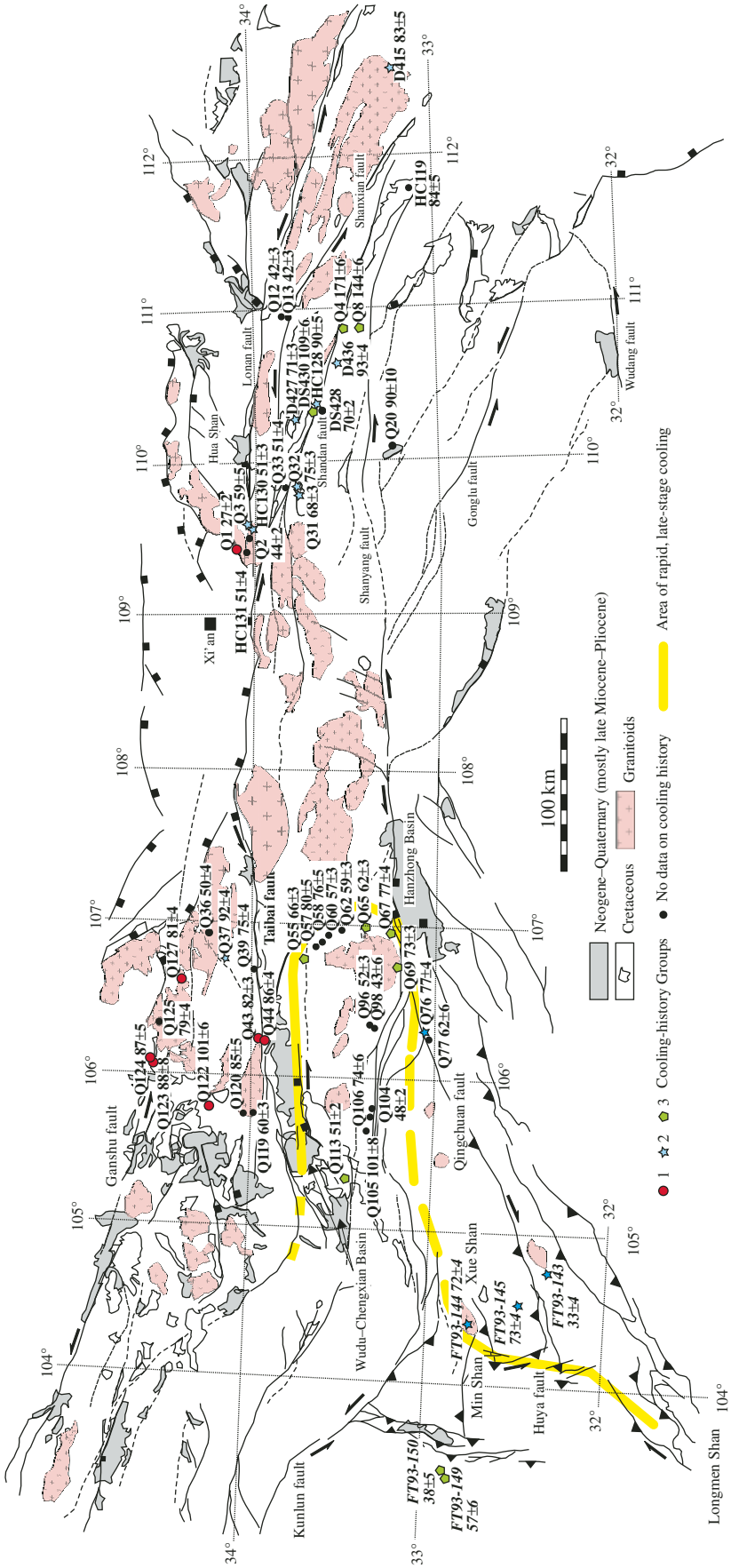

Figure 3. Compilation of likely Cenozoic faults in northeastern Tibet and the Qinling, and fission-track ages (in Ma with 1σ error) of the Qinling (this study) and of the area around the Min Shan (from Arne et al., 1997). Data not classified into cooling-history groups (see text) did not provide sufficient confined track-length data for discrimination.

ages between 88 and 76 Ma, and a narrow distribution with mean track lengths ≥13 μm, indicate rapid cooling during the Late Cretaceous and >4 km of exhumation, assuming a geothermal gradient of 30 ± 5 °C/km. T[t]-path models of samples Q123 and Q127 substantiate rapid cooling in the Late Cretaceous (Fig. 5A). Sample Q1, from west of Xi'an at the shoulder of the active Weihe graben, yielded the youngest fission-track age (27.3 ± 1.6 Ma) of this study. Its track-length distribution again indicates fast cooling (Fig. 5A).

Group 2 samples come from the eastern Qinling and the areas north of the Taibai (Q31, Q32, Q37) and south of the Qingchuan faults (Q76) in the western Qinling (Fig. 3). Most samples have Late Cretaceous ages and record continuous cooling (~1.2 °C/m.y.) since at least ca. 100–70 Ma. The negatively skewed track-length distributions are typical of continuous cooling since the time given by the fission-track ages; the uniformity, rather than the rate of cooling, is the decisive factor in producing this kind of distribution (Gleadow et al., 1986). T[t]-path models of samples Q31, D427, and D436 also highlight continuous cooling since the Early Cretaceous (D436; 120–100 Ma; Fig. 5B) and the Late Cretaceous (Q31 and D427; 85–70 Ma; Fig. 5B). Samples from the Kuanping unit of the North China Craton (Q2, Q3, Q12, Q13, HC130,

TABLE 1. APATITE FISSION-TRACK DATA, ROCK TYPE, AND SAMPLE LOCATION

Sample	Lithology	Latitude (N)	Longitude (E)	Grain	N_s	N_i	ρ_d (10^5 cm^{-2})	ϕ (10^{15} cm^{-2})	Z (10^8 year)	ζ (year cm^2)	P (χ^2)	ϕ age (Ma)	Z age (Ma)	ζ age (Ma)
Q 1	Granite	34°07.727′	109°25.628′	32	489	1112	4.49	2.02	1.17	282	0.06	27.3 ± 1.6	25.7 ± 1.4	27.9 ± 1.6
Q 2	Syenite	34°03.750′	109°29.678′	28	1099	1674	4.73	2.19	1.25	282	0.5	44.2 ± 1.9	40.9 ± 1.6	43.6 ± 2.1
Q 3	Gneiss	34°02.519′	109°35.062′	26	631	741	4.73	2.18	1.25	282	0.05	58.5 ± 4.6	53.0 ± 2.9	56.5 ± 3.5
Q 4	Metavolcanic	33°31.080′	110°52.611′	29	1873	727	4.73	2.18	1.25	282	0.30	171 ± 8	159 ± 7	170 ± 9
Q 8	Metavolcanic	33°26.081′	110°53.764′	29	2211	1017	4.73	2.18	1.25	282	0.06	144 ± 6	135 ± 5	143 ± 7
Q 12	Gneiss	33°52.771′	110°58.968′	25	826	1388	4.73	2.17	1.25	282	0.02	42.4 ± 2.7	39.6 ± 2.5	42.3 ± 2.6
Q 13	T sandstone	33°51.222′	110°58.842′	20	1142	1776	4.73	2.17	1.25	282	0.02	42.0 ± 2.6	39.4 ± 2.4	42.0 ± 2.6
Q 20	Granite	33°15.906′	111°08.903′	35	359	336	4.65	2.12	1.26	282	0.00	90.0 ± 10	86.7 ± 10	90.8 ± 11
Q 31	Diorite	33°46.315′	109°50.027′	14	1903	1852	4.73	2.16	1.25	282	0.12	68.0 ± 2.6	63.9 ± 2.1	68.2 ± 2.9
Q 32	Gneiss	33°49.485′	109°50.631′	20	1402	1236	4.73	2.15	1.25	282	0.17	74.9 ± 3.3	70.5 ± 2.8	75.2 ± 3.6
Q 33	Gneiss	33°51.464′	109°50.228′	20	1785	2338	4.73	2.15	1.25	282	0.00	51.0 ± 4.4	47.1 ± 4.1	51.4 ± 4.4
Q 36	Syenite	34°14.836′	106°56.149′	14	340	411	3.89	2.12	1.12	287	0.93	50.1 ± 3.8	46.3 ± 3.4	46.0 ± 4.7
Q 37	Diorite	34°09.079′	106°45.767′	22	1828	1198	3.89	2.11	1.12	287	0.94	91.7 ± 3.9	85.2 ± 3.2	84.6 ± 6.7
Q 39	Phyllite	34°02.006′	106°40.689′	8	852	686	3.89	2.10	1.12	287	0.26	74.5 ± 4.1	69.4 ± 3.6	69.0 ± 6.0
Q 43	Granodiorite	33°56.876′	106°18.007′	21	1996	1455	3.89	2.09	1.12	287	0.82	81.9 ± 3.3	76.6 ± 2.7	76.1 ± 5.9
Q 44	Metavolcanic	33°56.479′	106°17.849′	13	1417	976	3.89	2.09	1.12	287	0.32	86.3 ± 4.0	81.1 ± 3.4	80.5 ± 6.6
Q 55	Granodiorite	33°42.945′	106°47.103′	25	1221	1075	3.99	1.98	1.09	267	0.35	66.1 ± 3.1	60.4 ± 3.3	66.5 ± 3.4
Q 57	Tonalite	33°41.587′	106°48.197′	30	1348	1074	3.99	1.97	1.09	267	0.00	80.1 ± 5.1	75.2 ± 4.7	73.2 ± 4.6
Q 58	Tonalite	33°40.840′	106°49.862′	15	1515	1210	3.99	1.97	1.09	267	0.00	75.5 ± 4.6	71.2 ± 4.3	69.3 ± 9.2
Q 60	Granodiorite	33°38.064′	106°54.381′	19	1159	1117	3.99	1.96	1.09	267	0.02	57.0 ± 3.4	53.9 ± 3.2	52.5 ± 3.1
Q 62	Granodiorite	33°32.338′	106°58.743′	30	1132	1093	3.99	1.95	1.09	267	0.59	59.3 ± 2.8	56.4 ± 2.4	54.9 ± 5.0
Q 65	Migmatite	33°23.738′	106°59.816′	17	1363	1247	3.99	1.94	1.09	267	0.80	62.3 ± 2.7	60.1 ± 2.1	57.9 ± 5.1
Q 67	Diorite	33°15.184′	106°57.379′	17	1633	1158	3.99	1.93	1.09	267	0.02	76.6 ± 4.0	73.4 ± 3.8	71.4 ± 3.7
Q 69	Granite	33°12.838′	106°44.709′	15	1353	1048	3.99	1.92	1.09	267	0.83	75.7 ± 2.7	70.2 ± 2.9	68.3 ± 6.1
Q 76	Granite	33°03.296′	106°18.851′	28	1396	1027	3.99	1.92	1.09	267	0.06	76.5 ± 3.5	73.9 ± 3.0	71.9 ± 6.5
Q 77	Metavolcanic	33°01.083′	106°15.693′	25	263	238	3.99	1.91	1.09	267	0.83	62.0 ± 5.7	60.1 ± 5.4	58.5 ± 7.0
Q 96	Granite	33°21.698′	106°21.673′	19	566	612	3.99	1.9	1.09	267	0.07	51.7 ± 3.2	50.4 ± 2.9	49.0 ± 4.8
Q 98	Gabbro	33°21.191′	106°21.787′	27	105	136	3.99	1.89	1.09	267	1.00	43.0 ± 5.7	42.1 ± 5.5	41.0 ± 6.2
Q 104	Dike	33°20.177′	105°50.887′	36	861	1005	3.99	1.88	1.09	267	0.65	47.5 ± 2.8	46.7 ± 2.2	45.4 ± 4.2
Q 105	Dike	33°20.571′	105°48.372′	19	455	248	3.99	1.87	1.09	267	1.00	101 ± 8.2	99.6 ± 7.9	96.9 ± 11
Q 106	Dike	33°20.812′	105°45.634′	28	353	261	3.99	1.87	1.09	267	0.98	74.2 ± 6.2	73.5 ± 6.0	71.6 ± 8.2
Q 113	K_2 conglomerate	33°28.262′	105°21.860′	22	1109	1378	4.11	2.14		267	0.90	50.7 ± 2.3	N.D.	44.0 ± 2.2
Q 119	Granodiorite	33°57.529′	105°47.412′	17	1096	1089	3.89	2.08	1.12	287	0.11	59.7 ± 2.8	56.3 ± 2.4	55.9 ± 4.6
Q 120	Granodiorite	34°03.158′	105°45.494′	19	932	649	3.89	2.07	1.12	287	0.97	84.7 ± 4.7	80.2 ± 4.1	79.7 ± 6.9
Q 122	Metavolcanic	34°13.118′	105°48.056′	9	754	439	3.89	2.06	1.12	287	0.72	101 ± 6.4	95.8 ± 5.8	95.2 ± 8.8
Q 123	Granodiorite	34°32.555′	106°06.239′	15	1045	749	3.89	2.05	1.12	287	0.00	87.6 ± 8.3	83.5 ± 7.9	83.0 ± 7.8
Q 124	Gneiss	34°32.781′	106°11.538′	34	844	566	3.89	2.05	1.12	287	0.79	86.9 ± 5.0	83.3 ± 4.5	82.7 ± 7.3
Q 125	Syenite	34°30.770′	106°21.671′	15	1114	819	3.89	2.04	1.12	287	0.45	79.0 ± 4.0	76.0 ± 3.5	75.5 ± 6.3
Q 127	Diorite	34°22.191′	106°42.751′	24	1235	879	3.89	2.03	1.12	287	0.90	81.3 ± 3.9	78.5 ± 3.5	78.0 ± 6.5
D 415	Granite	33°17.164′	112°36.846′	31	727	604	5.01	2.31	1.42	278	0.13	82.6 ± 4.8	84.9 ± 4.9	83.3 ± 5.6
D 427	Gneiss	33°48.579′	110°15.976′	20	1951	1735	4.65	2.13	1.26	282	0.00	71.0 ± 2.7	70.3 ± 2.3	73.6 ± 3.1
D 436	Gneiss	33°32.743′	110°38.927′	21	1977	1329	4.65	2.12	1.26	282	0.81	93.6 ± 3.8	92.8 ± 3.3	96.8 ± 4.3
HC 119	K_1 sandstone	33°08.585′	111°45.352′	25	1161	1605	0.62	3.70	2.14	341	0.01	83.7 ± 4.5	79.8 ± 4.3	79.0 ± 4.2
HC 128	Granite	33°40.048′	110°21.232′	9	646	791	0.62	3.64	2.14	341	0.74	89.5 ± 5.1	86.8 ± 5.8	85.9 ± 4.8
HC 130	Granite	34°02.451′	109°34.221′	24	712	1516	0.62	3.61	2.14	341	0.50	51.2 ± 2.5	50.1 ± 3.0	49.5 ± 2.4
HC 131	Granite	34°04.461′	109°25.507′	26	324	692	0.62	3.59	2.14	341	1.00	50.8 ± 3.6	49.9 ± 3.9	49.4 ± 3.4
DS 428	Mylonite	33°39.752′	110°20.153′	40	2670	2813	3.87	2.46	1.53	369	0.21	70.4 ± 2.4	72.2 ± 3.3	68.6 ± 2.2
DS 430	Granite	33°42.325′	110°20.549′	40	3268	2318	3.87	2.45	1.53	369	0.00	109 ± 6	112 ± 6	105 ± 5

Note: N_s—number of spontaneous tracks; N_i—number of induced tracks; ρ_d—track density in standard uranium glass; ϕ—thermal neutron fluence; Z—Z calibration factor; ζ—ζ calibration factor; P[χ^2]—chi-square probability; T—Triassic; K_1—Early Cretaceous; K_2—Late Cretaceous.

HC131), located between the Lonan fault in the north and the Shanxian fault in the south, yielded Eocene apatite fission-track ages (Fig. 3). They record higher cooling rates (~2.0 °C/m.y.) than the other group 2 samples. Except for sample Q3 (Fig. 5B), we have no track-length information from this area because of low spontaneous track densities and small grain yield.

Samples of cooling group 3 are confined to the area between the Hanzhong and the Wudu–Chengxian Basins in the southwestern Qinling (Fig. 3). This region contains predominantly rocks of the Paleozoic–Mesozoic suture between North and South China (including Songpan–Garzê belt sedimentary rocks) plus minor allochthonous South China Craton basement and cover; Triassic granitoids that intruded these units imposed thick contact aureoles (BGMRSX, 1989, and our unpublished work). The symmetric track-length distributions of group 3 samples result from either of two possible thermal histories (Fig. 5C): (1) rapid cooling to ambient temperatures and prolonged steady state at ambient temperatures, followed by reheating to >60 °C that shortened all tracks at the end of the thermal history; (2) prolonged steady state or very slow cooling within the upper part of the PAZ, followed by rapid cooling to ambient temperatures at the very end of the thermal history; the latter kept the time span short for accumulating tracks at low temperatures. T[t]-path models for samples Q67 and Q69 give only broad envelopes of good-fit solutions (Fig. 5C) and indicate that thermal histories (1) and (2) are equally acceptable. Thermal history (2) is supported by T[t]-path modeling of sample Q65, which, using initial constraints between 85 and 75 Ma, produces a narrow range of good-fit solutions for very slow cooling within the PAZ, followed by rapid cooling at the end of the thermal history (Fig. 5C). Thermal history (2) is also more likely, because late reheating has not been reported from eastern Tibet and the Qinling. Samples Q4, Q8, and DS430 from the eastern Qinling (Fig. 3) yielded Jurassic to Early Cretaceous fission-track ages, indicating that exhumation in this area was <~4 km. Because these samples are surrounded by those of cooling group 2, their symmetric distribution is likely an effect of local Cenozoic faulting.

All of our thermal history models (Fig. 5) show a late thermal excursion into the PAZ that is likely an artifact caused by annealing at ambient temperatures acting over geological times. Low-temperature track-length reduction has been described for fossil tracks in age standards (Green, 1980, 1981, 1988; Watt et al., 1984; Watt and Durrani, 1985; Gleadow et al., 1986; Green et al., 1986; Donelick, 1991; Donelick et al., 1990) and borehole samples (Jonckheere and Wagner, 2000a). This reduction is not incorporated into the annealing equations derived

TABLE 2. RESULTS OF CONFINED TRACK-LENGTH MEASUREMENTS

Sample	MTL	Std.	Skewness	*N*
Group 1				
Q1	13.5	1.1	–0.10	42
Q43	12.8	1.1	–0.14	77
Q44	13.2	1.0	–0.27	15
Q122	13.1	1.0	–0.43	20
Q123	13.5	1.0	–0.41	156
Q124	12.9	0.8	–0.42	19
Q127	13.0	1.1	0.48	59
Group 2				
Q3	12.3	1.7	–0.62	40
Q31	13.2	1.4	–0.54	174
Q32	12.8	1.3	–0.90	68
Q37	12.9	1.3	–0.35	44
Q76	12.7	1.3	–0.44	30
D415	13.1	1.5	–0.80	120
D427	13.4	1.3	–0.21	157
D436	12.7	1.4	–0.30	250
HC128	12.5	1.6	–0.43	21
HC130	13.0	2.0	–1.08	12
Group 3				
Q4	12.1	1.1	0.02	58
Q8	12.2	1.4	–0.14	140
Q55	11.7	1.3	–0.13	112
Q65	11.9	1.6	–0.14	185
Q67	12.2	1.3	0.00	173
Q69	11.8	1.3	0.44	207
Q113	12.1	1.1	0.16	44
DS430	11.8	2.0	–0.29	89

Note: MTL—mean track length (μm); Std.—standard deviation; *N*—number of tracks; Skewness—asymmetry of unimodal frequency distribution to the mean.

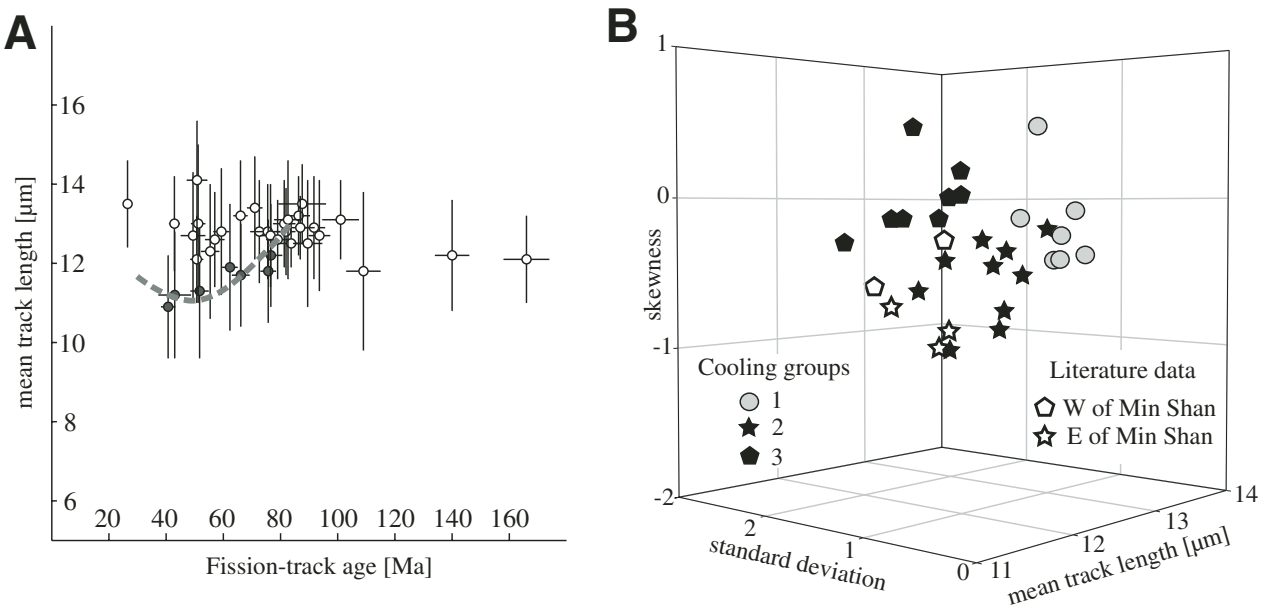

Figure 4. Cooling-history variations in the Qinling. (A) Fission-track ages plotted against their mean track lengths. Several samples with ages between 80 and 40 Ma and mean track lengths of >13 μm indicate rapid cooling at the time given by their age; they differ from samples of the same age group (black circles) that have a mean track length of <12 μm. The latter samples outline an incomplete boomerang (dashed gray line), suggesting a variety of cooling histories within the study area. (B) Relations between mean track length, standard deviation, and skewness highlight three different cooling-history groups (see also Fig. 5). Literature samples are from Arne et al. (1997; 2004, personal commun.).

Cooling History Group 1

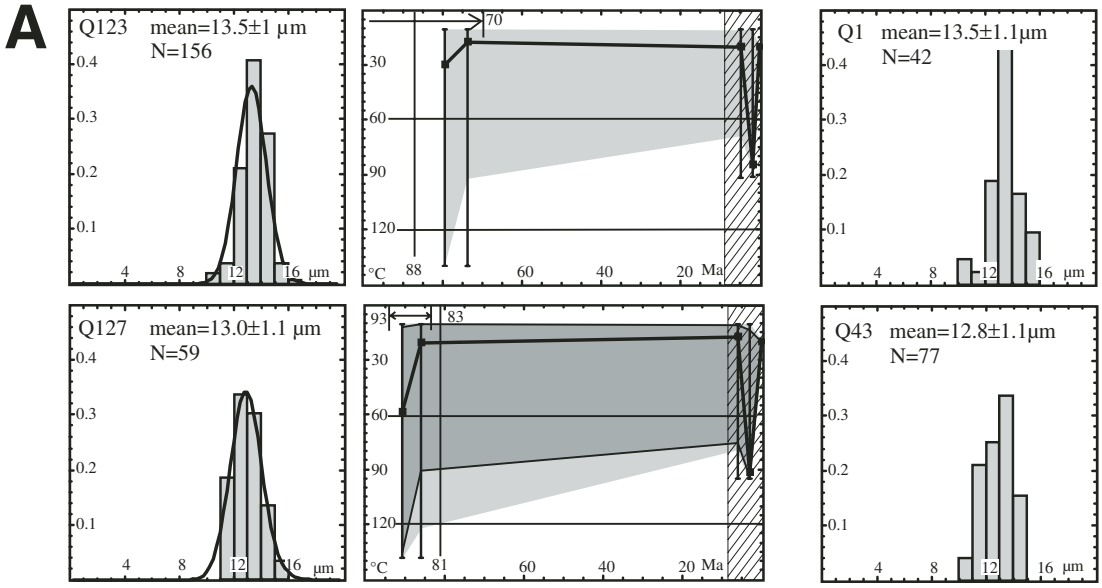

Cooling History Group 2

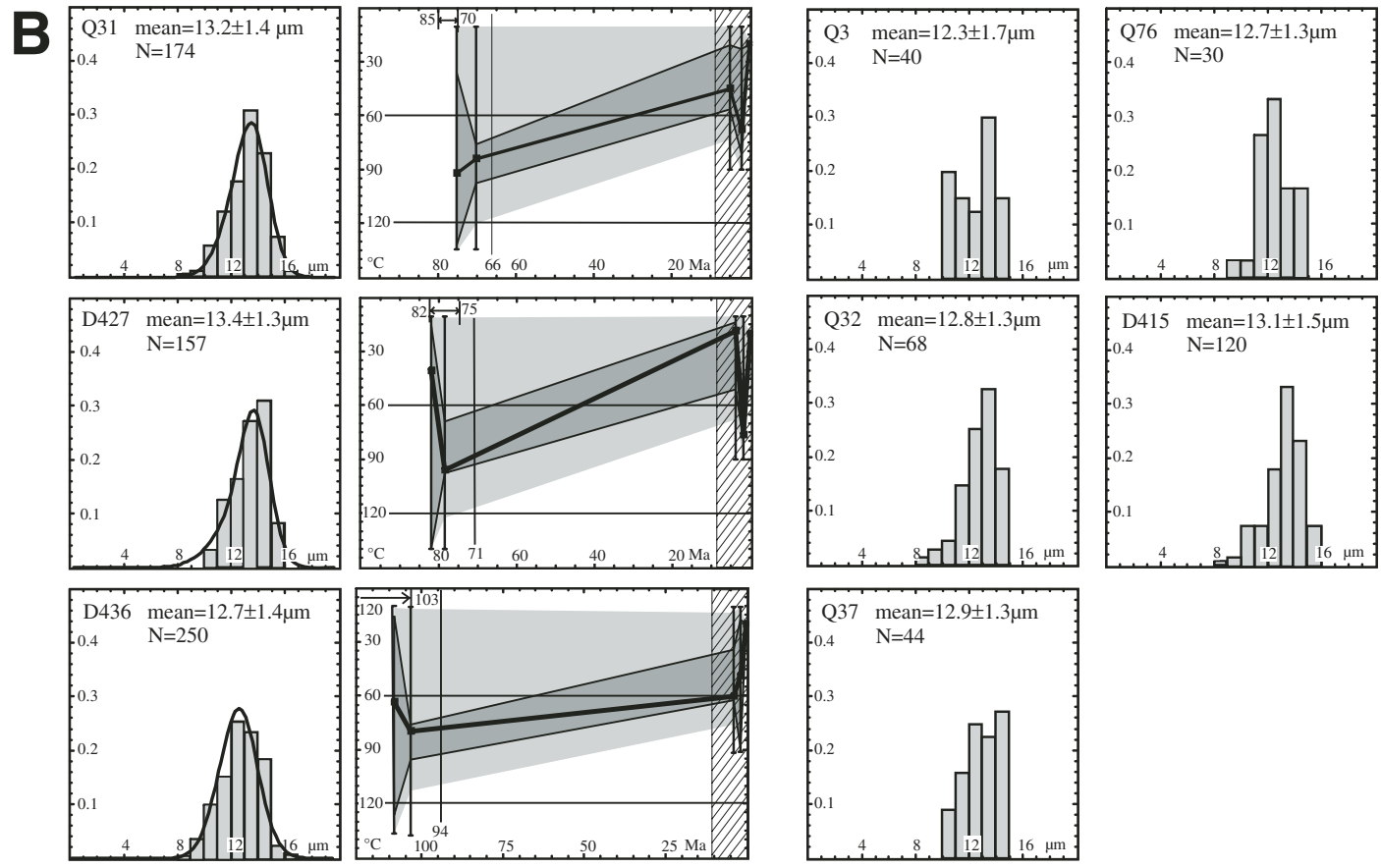

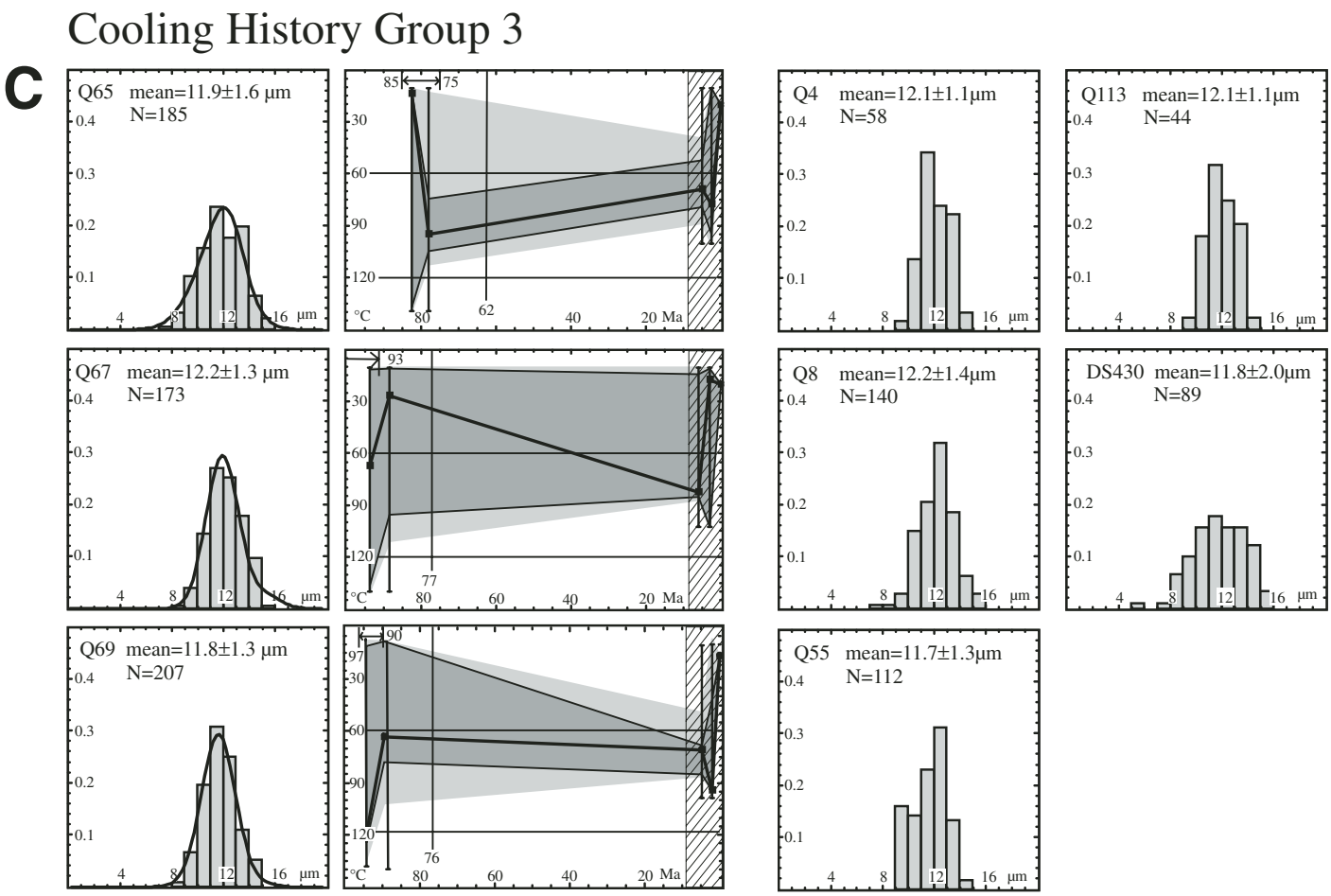

Figure 5 (*on this and previous page*). Confined track-length distributions of samples with >30 tracks and representative temperature-time (T[t]) paths for the three cooling-history groups defined by their length distributions (see Fig. 4 and text for details). Arrow and age numbers at the top of each T[t]-path diagram indicate the range of initial constraints for which the depicted T[t]-path solutions are valid. The constraints are represented by the bold vertical lines. Two closely spaced initial constraints allow the thermal histories to start with cooling or heating. Two constraints in the last few million years permit the model to find a thermal event (ruled box) that shortens all accumulated tracks and thus to account for track shortening at ambient temperatures over geological times (see text). The discussion in the text refers to the good-fit solutions (dark gray: all T[t]-paths with a merit function value of at least 0.5, Ketcham et al. [2000]); acceptable-fit solutions (light gray: all T[t] paths with a merit function value of at least 0.05) are shown for reference. Vertical line with the number at the bottom of each diagram gives the apatite fission-track age (Ma).

from laboratory annealing experiments on induced fission tracks, which account only for the annealing process that takes part within the PAZ (Jonckheere, 2003a, 2003b). We imposed two constraints in the last few million years of the T[t] paths to allow the model to find a thermal event (marked with a ruled box in the models of Fig. 5) that reduces all accumulated tracks, thus to account for the track shortening at ambient temperatures over geological times. For our cooling group 3 samples, however, it is likely that this artifact veils a real phase of late, rapid cooling after a prolonged period of track accumulation at temperatures of accelerated track annealing, indicated by the lack of long, un-annealed tracks. The artifact precludes the exact determination of the onset of this rapid terminal cooling using T[t]-path modeling. Nevertheless, attempts have been reported to extract information about the cooling history through a careful analysis of track-length distributions (e.g., Wagner, 1988; Wagner et al., 1989; Belton et al., 2004). Here, we estimate the onset of rapid cooling in our cooling group 3 samples by dividing the track-length distribution into tracks formed at temperatures of accelerated annealing known as the PAZ (60–120 °C) and those formed at low temperatures (<60 °C) with little track shortening having acted over geological times (Fig. 6). Using the linear relationship between the fission-track age and the number of tracks, we calculate the time necessary to produce the number of tracks at low temperatures; we suggest that this time corresponds to the onset of rapid cooling as indicated in Figure 6. The calculation is detailed in Appendix 1. For samples Q65, Q67, and Q69, which have a high number of measured confined tracks, the onset of rapid cooling was at ca. 9–4 Ma (Table A1).

FAULTING IN THE WESTERN QINLING

Our work on Cenozoic faulting in the western Qinling builds on studies elucidating the

early Mesozoic evolution of the Qinling–Dabie orogenic belt (e.g., Hacker et al., 2000; Ratschbacher et al., 2003). In the course of these studies, we addressed the Cretaceous and Cenozoic overprint in reconnaissance. Here, we first compiled likely Cenozoic faults in northeastern Tibet and the Qinling by reevaluating Chinese geologic maps. We then modified this compilation by incorporating published studies (Kirby et al., 2000; Zhang et al., 1998; Gaudemer et al., 1995; Lasserre et al., 1999; Burchfiel et al., 1995; Peltzer et al., 1985; Ratschbacher et al., 2003) and our field work interpretations (Fig. 2). Next, we characterized the regional deformation field by mesoscale fault-slip analysis ("paleostress studies"; e.g., Angelier, 1994). Appendix 2 summarizes our approach to fault-slip analysis and the definition of stress groups in the brittle crust and reviews the applied calculation techniques. Critical to the establishment of regional stress fields is the recognition of consistent superposition criteria between fault subsets on a regional scale. For relative age criteria, we relied on classic overprinting relationships (Appendix 2; Fig. 2). Our apatite fission-track thermochronology and (sporadic) stratigraphic data (Wudu-Chengxian Basin; see the following) provided absolute time constraints. The regional stress-axes distribution plotted in Figure 2 most likely encompasses the Neogene–Holocene. This is because the related fault sets represent the final increments in the relative faulting chronology, and the associated deformation fabrics signify near-surface conditions (e.g., faults associated with weakly consolidated cataclastic rocks and Holocene geomorphologic features), thus postdating the time given by the apatite fission-track ages. Although refinement of this data set awaits detailed neotectonic studies, the regional variation is significant, and the superposition of faulting events, a key to our interpretation, is reliable.

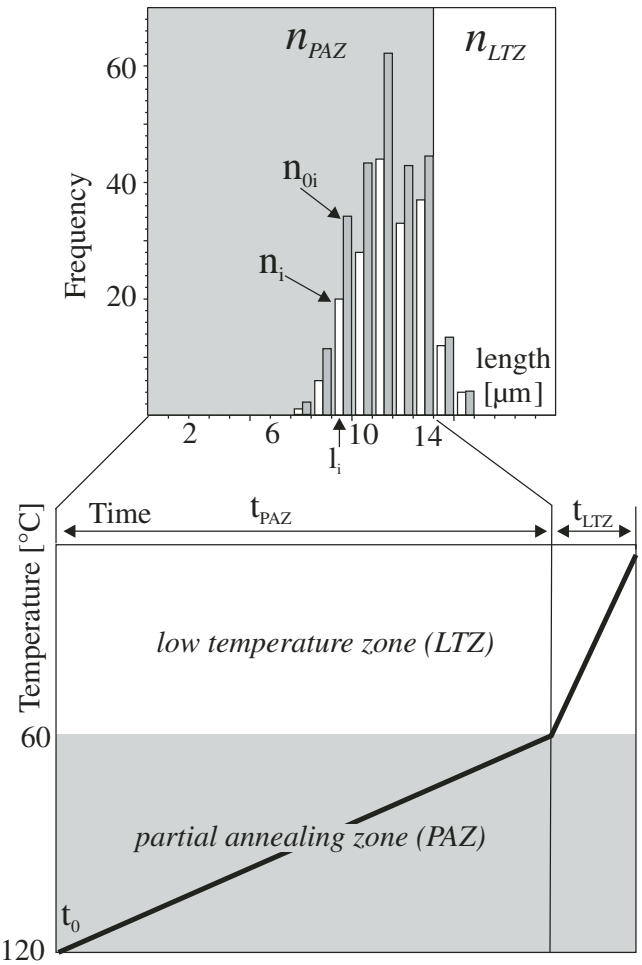

Figure 6. Sketch of principle underlying calculation of onset of rapid cooling from well-defined track-length distributions (see Appendix 1 for explanations). Top: measured (white) and corrected (gray) track-length distribution of sample Q65. Bottom: sketch of the partial annealing zone (PAZ) and the low temperature zone (LTZ) of apatite and the relationship between the T[t] path of the sample and the resulting track-length distribution. Explanation: n_i—number of measured tracks with track length, l_i; n_{0i}—corrected number of tracks; t_{PAZ}—residence time of the sample in the PAZ; t_{LTZ}—residence time of the sample in the LTZ; n_{PAZ}—number of tracks formed in the PAZ; n_{LTZ}—number of tracks formed in the LTZ.

Bellier et al. (1988, 1991), Zhang et al. (1995, 1998, 2003), Grimmer et al. (2002), and Ratschbacher et al. (2003) established three Cenozoic stress fields (Paleogene, likely Neogene, and "neotectonic") in the Weihe graben and the eastern Qinling-Dabie Shan–Tan-Lu fault region. Evidence of these stress fields was also found in the western Qinling. In the following, we elaborate on the "neotectonic" field and discuss four areas, the eastern Qinling, the Longmen Shan and Min Shan, the northern Qinling, and the southwestern Qinling.

The eastern Qinling shows sinistral strike-slip deformation distributed over a north-south distance of at least 250 km; displacement is concentrated along the Lonan and Shandan fault systems (Peltzer et al., 1985; Ratschbacher et al., 2003). The orientation of the neotectonic stress field is well established (σ_1 = 048 ± 10°; Fig. 2). Few quantitative data on the neotectonic stress field of the Longmen Shan and the Min Shan are available. Twenty-six stations from the southern Longmen Shan and the easternmost Songpan-Garzê belt (Ratschbacher et al., 1996; Wilson et al., 2005) gave an east-southeast–trending σ_1 (107 ± 32°, Fig. 2). This field imposes a dextral strike-slip component onto neotectonic thrusts in the Longmen Shan that is also inferred from geodetic studies (Chen et al., 2000). Focal mechanisms of the 1976 Songpan earthquakes gave similar stress orientations and demonstrate active deformation in the Min Shan (Fig. 2; Jones et al., 1984; Kirby et al., 2000). The neotectonic field overprints an older field with northeast-trending σ_1 (Ratschbacher et al., 1996).

All stations in the western Qinling share a neotectonic stress field with northeast-trending σ_1 (062 ± 13°; Fig. 2); faulting is overwhelmingly sinistral strike slip along roughly east-striking planes. In the northwestern Qinling, those stations that record an evolution in faulting mode suggest that normal faulting preceded strike-slip faulting (Figs. 2, 7). The major fault in the northwestern Qinling is the Taibai fault. It is associated with the Neogene–Holocene Wudu-Chengxian Basin, which overprints a larger Cretaceous basin. Station Q116, measured in mostly Neogene rocks, shows block tilting induced by normal faulting (Fig. 7A).

Several faults at this station also cut likely Pleistocene loess (compare the Weihe graben; Zhang et al., 1998), indicating that the last faulting increment in the Wudu-Chengxian Basin has normal geometry; the master fault is likely along the southern basin margin. The Hanzhong Basin, likely mainly of late Miocene–Pliocene age, is the major structural feature of the central to western Qinling; predominantly normal faults rim its northern margin (Figs. 2, 7). The basin formed either by sinistral strike slip along approximately west-northwest–striking faults entering the basin from the west or by dextral strike slip along the northeast-striking Qingchuan fault system (Fig. 2).

Both models contain unexplained aspects: although the Qingchuan fault is an outstanding morphological feature on maps and satellite images, and clearly affects river drainage (the largest dextral offset along the Jialing River is ~15 km, Fig. 2), geodetic results (Chen et al., 2000; King et al., 1997) suggest that active dextral displacement on the fault is restricted to a few millimeters per year. Furthermore, the fault apparently does not connect to one of the main faults of the Longmen Shan, making large-scale dextral displacement unlikely (see also Kirby et al., 2000). Likewise, no first-order connection between the sinistral west-northwest–striking faults west-northwest of the Hanzhong Basin and either the Kunlun fault or other faults north of it (Fig. 2) is apparent along the northern margin of the Xue Shan and the southern rim of the Wudu-Chengxian Basin. Significantly, however, our data provide clear evidence for late-stage dextral wrenching (stations Q73–75, Q81, Q85; latest deformation increment; Figs. 2, 7) along the Qingchuan and related faults south and east of the Xue Shan, overprinting the earlier regional, dominantly sinistral wrenching (Fig. 2). During this latest deformation increment, dextral strike-slip faulting is associated with thrusting north of the Hanzhong Basin (station Q67–68; Figs. 2, 7) and normal faulting along one of the faults bordering the basin (station Q72; Figs. 2, 7). The maximum principal stress, σ_1, trends west-northwest (116° ± 14°) for this faulting increment and is thus identical to the active deformation inferred for the Longmen Shan and Min Shan (Fig. 2).

DISCUSSION

Rapid Late Cretaceous Exhumation in the Northwestern Qinling

In the eastern Qinling, Late Cretaceous–Eocene basins are associated with west-northwest–trending dextral strike-slip fault zones and a stress field with northeast-southwest extension and northwest-southeast compression; K-feldspar cooling ages bracket this faulting between ca. 101 Ma and 63 Ma (Ratschbacher et al., 2003). Farther east, the Dabie Shan was reheated at ca. 100–90 Ma, and the west-northwest–trending Xiaotian-Mozitang fault zone was dextral and probably conjugate to the sinistral-transtensive Tan-Lu fault zone (Ratschbacher et al., 2000), for which fault gouge yielded 110–90 Ma ages along strands far north of Dabie (Chen et al., 1990). A broad dextral shear belt occupies the eastern Tongbai Shan between the Qinling and Dabie; at least locally, this shear belt was reactivated at ca. 75 Ma (Webb et al., 1999, 2001). Most of the apatite fission-track ages from Dabie are Late Cretaceous (Grimmer et al., 2002; Reiners et al., 2003). Cretaceous sedimentary rocks also occur throughout the western Qinling, mostly in elongated basins along west-northwest–trending strike-slip faults (Fig. 2); in particular, Late Cretaceous–Eocene sedimentary rocks crop out along the Ganshu fault (BGMRSX, 1991).

Most of our apatite fission-track samples record Late Cretaceous–Eocene cooling with variable amounts of exhumation in the Qinling. Cooling-history group 1 samples indicate rapid cooling to ambient temperatures (exhumation of ≥4 km, assuming a geothermal gradient of 30 ± 5 °C/km) in the Late Cretaceous followed by steady state at low temperatures throughout the Tertiary (Figs. 3, 5). They occur along the Ganshu fault, along the northern margin of the western Qinling, and along the Taibai fault, and thus overlap the area of Late Cretaceous–early Tertiary basin formation. We suggest that the northwest-southeast compressional and northeast-southwest extensional stress field, characteristic of all of eastern China from the late Early Cretaceous to the late Late Cretaceous (Ratschbacher et al., 2003), was associated with strike-slip faulting and basin formation in the western Qinling and is dated by our group 1 fission-track ages. Samples of cooling groups 2 and 3 signify that other areas within the Qinling have been less affected by exhumation in the Late Cretaceous–Eocene and that these samples were exposed to temperatures where partial track annealing has occurred (~120–60 °C) (see the following).

Continuous, Slow Exhumation and Peneplanation in the Tertiary

Slow exhumation from the Cretaceous to the Miocene is known from the eastern Tibetan Plateau and the area north of the Kunlun fault zone: on the basis of apatite fission-track T[t]-path modeling, Arne et al. (1997) proposed very slow cooling from the Cretaceous to ca. 20 Ma for the Longmen Shan. Roger et al. (2004) advocated very slow cooling from ca. 150 to 25 Ma from U/Pb and Rb/Sr data from Indosinian granites in the Songpan-Garzê fold belt. Using $^{40}Ar/^{39}Ar$ K-feldspar and (U-Th)/He zircon and apatite thermochronology data, Kirby et al. (2002) suggested slow cooling (~3 °C/m.y.) in the interior of the Songpan-Garzê belt, with 1–2 km of exhumation from the Jurassic to the late Miocene or early Pliocene. They suggested that the very slow exhumation within the Songpan-Garzê belt, the northeastern Longmen Shan, and the area north of the Kunlun fault indicates a stable region characterized by insignificant exhumation and peneplanation, which formed the low-amplitude, long-wavelength topography of the eastern Tibetan Plateau (e.g., Kirby et al., 2002; Schoenbohm et al., 2004). Their data indicate that this surface formed prior to the middle Miocene. Cooling-history group 2 samples from the eastern Qinling, from north of the Taibai fault in the northwestern Qinling, and from south of the Qingchuan fault in the southwestern Qinling, also record continuous, slow cooling (~1.2 °C/m.y.) since at least 100–70 Ma; T[t]-path modeling suggests it persisted throughout the Tertiary (Fig. 5). Samples from the northeastern Qinling, between the Lonan and Shanxian faults, record faster but still moderate cooling rates (~2.0 °C/m.y.).

Cooling-history group 3 samples differ from those of group 2 by indicating rapid, late-stage cooling; both groups share the same continuous, slow, Late Cretaceous–Tertiary cooling. Thus the entire western and eastern Qinling record the same continuous slow exhumation throughout the Late Cretaceous–Tertiary, albeit with at least locally slightly higher rates than that of the eastern Tibetan Plateau. As previously outlined, the Weihe graben, part of the Cenozoic graben system surrounding the Ordos Block, constitutes the northern edge of the central and eastern Qinling. After a slow start in the Eocene to early Oligocene, subsidence accelerated to a rate of ~0.20 mm/yr in the middle to late Miocene, and to ~1 mm/yr during the Quaternary (Bellier et al., 1988). The major faults bounding the eastern Weihe graben (east of Xi'an and along the Hua Shan; Fig. 2) have been active since 50–45 Ma and are linked with the Lonan and Shanxian faults (Peltzer et al., 1985; Zhang et al., 1995, 1998; Ratschbacher et al., 2003). Our youngest fission-track ages, and those indicating the highest cooling rates in the eastern Qinling, record this concentration of vertical displacement along the Weihe graben. The evolution of the Weihe graben also determined the topography and thus the evolution of the south-directed drainage system of the Qinling. It is likely that

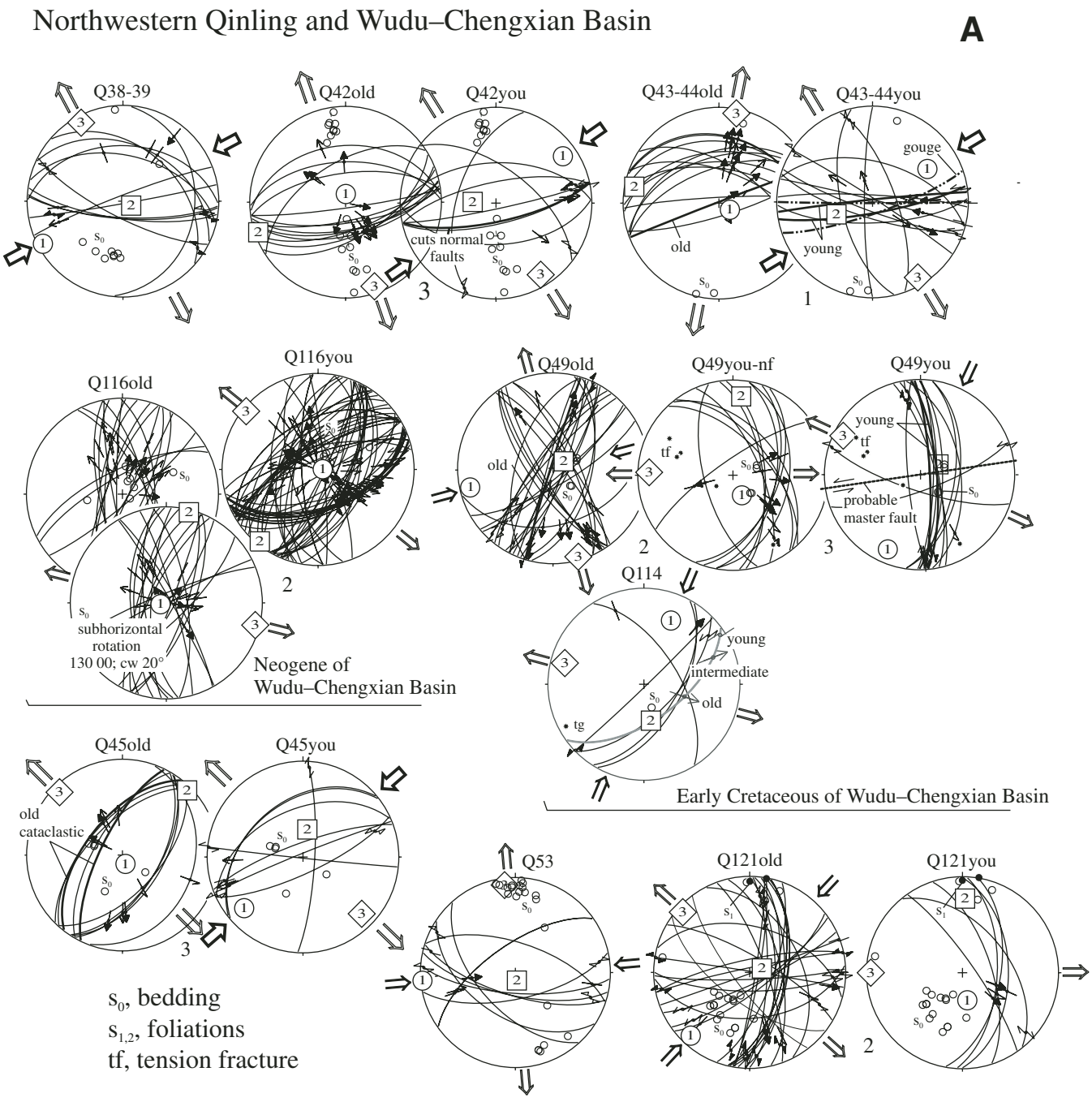

Figure 7. Lower-hemisphere, equal-area stereograms show fault-slip data and principal stress orientations (1, 2, and 3 denote σ_1, σ_2, and σ_3) plotted in Figure 2; faults are drawn as great circles, and striae as arrows pointing in the direction of displacement of the hanging wall. Confidence levels of slip-sense determination are expressed in the arrowhead style: solid, certain; open, reliable; half, unreliable; without arrowhead, poor. Arrows around the plots give calculated local orientation of subhorizontal principal compression and extension. Numbers between stereograms (1–3) give confidence levels (classified as above) for determining the relative age relationship between subsets; those without numbers have confidence level 4. See Table 3 and text for details. (*Continued on following page*.)

Southwestern Qinling – Xue Shan and Hanzhong Basin

B

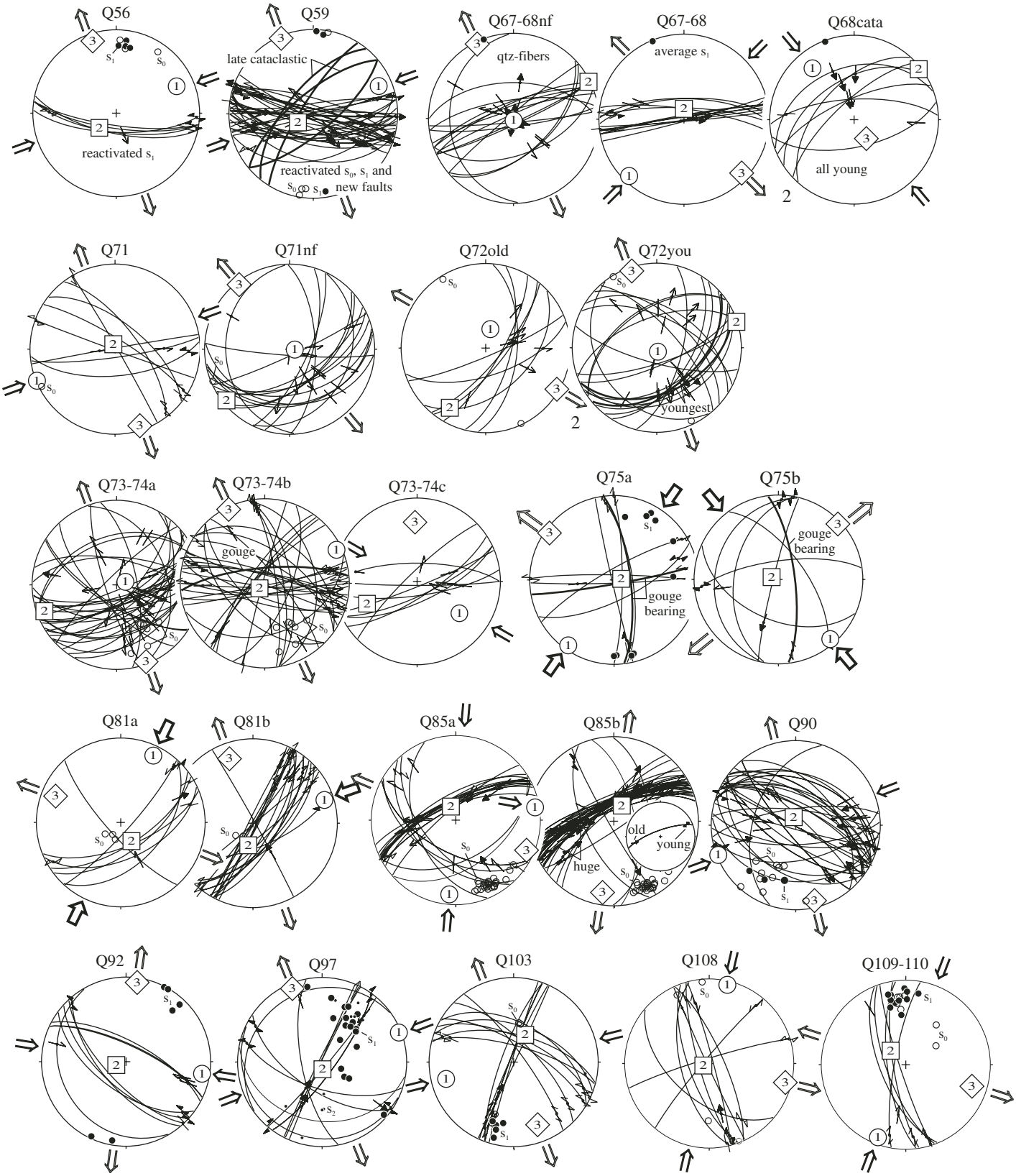

TABLE 3. LOCATIONS OF STATIONS AND PARAMETERS OF THE DEVIATORIC STRESS TENSOR

Site and Set name	Lithology	Latitude (N)	Longitude (E)	Method	*n*	σ_1	σ_2	σ_3	*F*	*R*
Q38–39	D_2-C_1 metasiltstone	34°04.485′–34°02.006′	106°43.240′–106°40.689′	NDA	11 11	242 05	118 82	332 07	28°	0.24
Q42you	D metasiltstone, metavolcanic	33°57.194′	106°17.943′	NDA	08 08	055 16	273 70	148 12	14°	0.5
Q42old	D metasiltstone, metavolcanic	33°57.194′	106°17.943′	NDA	13 13	002 83	251 03	161 07	8°	0.5
Q43–44old	D_2, metamorphic shale; T granitoid	33°56.876′–33°56.479′	106°18.007′–106°17.849′	NDA (45°)	14 14	121 79	281 10	011 04	11°	0.5
Q43–44you	D_2, metamorphic shale; T granitoid	33°56.876′–33°56.479′	33°56.876′–33°56.479′	NDA	13 13	056 42	261 45	158 13	21°	0.5
Q45you	T_2 shale and siltstone	33°56.209′	106°17.813′	NDA	08 07	229 19	009 66	134 15	18°	0.6
Q45old	T_2 shale and siltstone	33°56.209′	106°17.813′	NDA	10 10	161 82	045 04	315 07	15°	0.6
Q49old	K_1 conglomerate	33°53.670′–33°53.492′	106°27.051′–106°27.713′	PBT	26 25	257 11	057 79	164 03		
Q49you	K_1 conglomerate	33°53.670′–33°53.492′	106°27.051′–106°27.713′	PBT	13 12	203 15	060 72	297 10		
Q49you-nf	K_1 conglomerate	33°53.670′–33°53.492′	106°27.051′–106°27.713′	PBT	13 12	156 71	006 17	272 12		
Q53	T_1 shale	33°49.319′	106°35.603′	PBT	09 09	265 01	169 83	353 07		
Q56	D_3 limestone-marble	33°42.068′	106°47.474′	PBT	05 05	066 21	229 68	342 09		
Q59	D_2 marble-tectonite	33°39.084′	106°53.392′	NDA	40 39	67 16	241 73	337 02	24°	0.7
Q67–68nf	garnet–mica schist, ?D quartzite and schist	33°15.184′–33°13.636′	106°57.379′–106°57.678′	NDA	16 16	175 88	064 01	334 02	10°	0.45
Q67–68	garnet–mica schist, ?D quartzite and schist	33°15.184′–33°13.636′	106°57.379′–106°57.678′	NDA (45°)	11 11	224 07	360 80	133 07	35°	0.6
Q68cata	?D quartzite and schist	33°13.636′	106°57.678′	NDA	07 07	321 22	052 02	147 68	17	0.4
Q71nf	J_2 massive dolomite	33°12.093′	106°44.302′	NDA	16 16	094 85	231 04	322 03	19°	0.4
Q71	J_2 massive dolomite	33°12.093′	106°44.302′	PBT (45°)	08 08	248 00	341 85	162 05		
Q72you	J_2 limestone-shale sequence and fault breccia	33°12.397′	106°49.353′	NDA	20 20	163 86	072 00	342 04	14°	0.4
Q72old	J_2 limestone-shale sequence and fault breccia	33°12.397′	106°49.353′	PBT	08 08	014 71	211 18	120 02		
Q73–74a	?Sinian dolomite	33°07.812′–33°07.614′	106°33.155′–106°32.820′	PBT	33 33	071 81	250 09	159 02		
Q73–74b	?Sinian dolomite	33°07.812′–33°07.614′	106°33.155′–106°32.820′	NDA	32 32	065 06	226 83	334 02	19°	0.5
Q73–74c	?Sinian dolomite	33°07.812′–33°07.614′	106°33.155′–106°32.820′	PBT	08 08	127 36	246 34	358 29		
Q75a	?Cambrian shale	33°05.838′	106°26.666′	NDA	09 09	215 05	081 83	306 05	14°	0.55
Q75b	?Cambrian shale	33°05.838′	106°26.666′	PBT	07 07	139 06	289 83	047 03		
Q81a	?Cambrian dolomitic limestone	32°59.298′	106°15.363′	NDA	07 07	026 12	150 69	292 17	17°	0.5
Q81b	?Cambrian dolomitic limestone	32°59.298′	106°15.363′	NDA	19 18	072 12	191 67	338 20	07°	0.5
Q85a	?Sinian carbonate	33°06.701′	106°17.171′	PBT (40)	21 21	185 12	340 76	113 09		
Q85b	?Sinian carbonate	33°06.701′	106°17.171′	NDA (35)	39 38	280 05	027 74	189 15	34°	0.7
Q90	limestone	33°17.090′	106°13.311′	PBT (40)	32 32	249 01	346 82	166 08		
Q92	limestone	33°19.556′	106°13.180′	NDA (25)	08 08	099 09	251 80	008 05	11°	0.3
Q97	?S phyllite	33°21.437′	106°21.672′	NDA (35)	12 12	069 02	177 83	338 06	21°	0.5
Q103	?D radiolarian chert	33°21.387′	105°54.411′	NDA	14 14	256 18	023 61	159 21	11°	0.5
Q108	marble	33°19.451′	105°36.419′	NDA	09 09	013 04	251 84	104 07	17°	0.5
Q109–110	metavolcanic of basement	33°16.824′–33°17.323′	105°37.381′–105°37.343′	NDA (35)	08 08	201 08	313 70	108 18	17°	0.8
Q114	K_1 conglomerate	33°30.593′	105°21.999′	NDA	08 08	023 28	169 58	285 15	13°	0.5
Q116old	Neogene	33°48.384′	105°49.215′	NDA	19 18	257 85	014 02	104 04	14°	0.1
Q116you	Neogene	33°48.384′	105°49.215′	NDA	18 18	087 86	219 03	309 03	18°	0.5
Q121old	D_2 shale-sandstone sequence	33°57.376′	105°47.298′	PBT	27 26	223 10	072 79	312 06		
Q121you	D_2 shale-sandstone sequence	33°57.376′	105°47.298′	PBT	06 06	170 66	002 23	270 01		

Note: The numerical dynamic analysis method (NDA; Spang, 1972) and the P-B-T axes method (PBT; Turner, 1953) were used for calculation of principal stress directions ($\sigma_1 \geq \sigma_2 \geq \sigma_3$). In the measurement column *(n)*, the first number gives total number of measurements, and the second number is number of measurements used for calculation. For σ_1 to σ_3, azimuth (first number) and plunge (second number) of the principal stress axes are given. The stress ratio, *R*, is $(\sigma_2 - \sigma_3)(\sigma_1 - \sigma_3)^{-1}$. The fluctuation, *F*, gives the average angle between the measured slip and the orientation of the calculated theoretical shear stress. D—Devonian; C—Carboniferous; T—Triassic; J—Jurassic; K—Cretaceous; $_1$, $_2$—early and late epochs of the period. ? in front of epoch indicates site whose stratigraphic age we do not regard as firmly established; you—young; nf

the rivers of the Qinling were part of the large-scale, dendritic, low-relief, continental-interior type of drainage system that may have existed before the mid-Miocene–Holocene uplift of the eastern Tibetan Plateau (Clark et al., 2004) and the southwestern Qinling (see the following discussion). The initiation of the Weihe graben in the early Tertiary, and thus the earlier onset and the less-focused exhumation in the Qinling rather than within eastern Tibet, may be responsible for the apparent lack of preservation of the "relict landscape," so well preserved in the interior of the eastern Tibetan Plateau (Schoenbohm et al., 2004).

Late Cenozoic Rapid Exhumation in Southwestern Qinling

Samples from the southwestern Qinling, between the Hanzhong and the Wudu-Chengxian Basins, record symmetric length distributions (group 3 cooling histories) and signify rapid cooling from the upper PAZ (90–60 °C) to ambient temperatures at the very end of the thermal history (area outlined in Fig. 3). Assuming a geothermal gradient of 30 ± 5 °C/km, the late-stage cooling corresponds to an exhumation of 2–3 km. The time of initiation of rapid exhumation is, in principle, preserved in the track-length distributions of the relevant samples, but owing to the artifact discussed earlier, an exact age estimate using T[t]-path modeling is impossible. A rough estimate based on the track-length distribution of three samples points to a late Miocene–early Pliocene (9–4 Ma) onset of rapid cooling; this is consistent with the late Miocene–Pliocene sedimentation in the Cenozoic basins of the Qinling (e.g., the Hanzhong and Wudu-Chengxian Basins).

Exhumation in the Min Shan and in the plateau to its west and southwest started in the mid-Miocene (Enkelmann et al., 2004). Symmetric length distributions similar to those in the

southwestern Qinling also occur in samples from west of the Min Shan (FT93-149, FT93-150 of Arne et al., 1997) and are plotted in Figure 4B together with the Qinling samples. The former correspond to the group 3 cooling history of the southwestern Qinling. Their ages are younger (57–38 Ma), however, implying that exhumation started earlier and was stronger than in the southwestern Qinling; this independently constrains the onset of rapid, late-stage exhumation in the southwestern Qinling to have been late Miocene or younger. Late Cretaceous to early Paleocene ages (80–63 Ma), similar to those of the southwestern Qinling, also occur north of the Kunlun fault zone in the westernmost Qinling (Enkelmann et al., 2004). Unfortunately, the small number of grains and low spontaneous track densities prohibit assessment of the cooling behavior. The boundary between the area of rapid, late-stage exhumation in the southwestern Qinling and the area north of it is thus poorly defined and awaits more thermochronology west of the Wudu-Chengxian Basin and in northeastern Tibet. The Huya and Qingchuan fault zones delimit the Xue Shan from the Min Shan and the northeastern Sichuan Basin, respectively. Apatite fission-track ages from the western Xue Shan are 73–33 Ma and show the broad, skewed length distribution (Arne et al., 1997) of cooling group 2 and are similar to sample Q76 from south of the Qingchuan fault (Figs. 3, 4B). Apparently, the allochthonous South China Craton basement of the Xue Shan has not yet been affected by the rapid, late-stage exhumation shown by apatite fission-track thermochronology in eastern Tibet and the southwestern Qinling.

We emphasize that, with fission-track data alone, we cannot rule out that the late Cenozoic rapid exhumation did not affect the entire Qinling; however, if it occurred, it was less (<1 km) than in the area outlined by samples of cooling group 3 (Fig. 3). Note also that the major zones of late Miocene–Pliocene normal faulting and basin formation (normal fault zones delineating the Wudu-Chengxian Basin in the south and the Hanzhong Basin in the north) not only support exhumation of the region occupied by the cooling group 3 samples but also suggest that late-stage exhumation is focused on the southwestern Qinling.

What caused the rapid, late-stage exhumation in the southwestern Qinling, and how is it related to the growth of the Tibetan Plateau? Incorporating other, in particular our fault-slip, data, we discuss two interpretations. Figure 8A outlines boundary conditions that are likely important in both models—i.e., the location of the southern and northern rims of the exposed basement of the North and South China Cratons, the major fault zones, the location of the steep plateau margin that loses its abruptness north of the Min Shan, and the area of rapid, late Cenozoic exhumation defined by our fission-track data (group 3 cooling histories).

Lower Crustal Flow Model

The lower crustal flow model (Fig. 8B) suggests that after encountering the rheologically strong basement of the Sichuan Basin along the Longmen Shan (cf. Clark and Royden, 2000), flow was diverted northeastward beneath the southwestern Qinling, following the rheologically "weak" crustal corridor along the Paleozoic–Mesozoic Qinling suture. Upper crustal responses to this flow beneath the Qinling may be the sinistral strike-slip faults along the Wudu-Chengxian Basin—i.e., the Taibai and related second-order faults—and the dextral strike slip along the Qingchuan fault zone. The disappearance of the steep topographic plateau margin north of the Min Shan is caused in this model by the rheological transition from the strong crust of the South China Craton to the weak crust of the Songpan-Garzê belt and the Qinling orogen. Uplift of the southwestern Qinling resulting from lower crustal flow may also be expressed in the late Miocene–Holocene sedimentation in the Hanzhong and Wudu-Chengxian Basins and the related normal faulting. The flow may have induced contraction at the eastern tip of the zone of rapid exhumation—i.e., north of the Hanzhong Basin. In this model, the eastward younging of the onset of rapid exhumation and the decrease in the amount of exhumation (from eastern Tibet into the Qinling) illuminate the eastward propagation of lower crustal flow.

Plateau Growth–Backstop Model

In the plateau growth–backstop model (Fig. 8C), rapid, late-stage exhumation in the southwestern Qinling has resulted from oblique thrusting-folding along the northwestern margin of the South China Craton and the narrowing of the corridor along which the northeastern Tibetan Plateau has been growing eastward. The rigid South China Craton acts as a backstop along which the shortening rate diminishes, and growth is channeled eastward. Geodetic studies (Chen et al., 2000; Zhang et al., 2004) indicate east(northeast)ward growth of the eastern Tibetan Plateau (in a Eurasian reference frame). Higher velocities in the northeastern part of the plateau than those within the Longmen Shan have induced clockwise material rotation in the northeastern plateau and the western Qinling. The geodetic data also imply that the northeastern Tibetan Plateau is currently growing faster eastward than the entire Southern China Craton is extruding to the east; this is compensated by shortening and uplift in the western Qinling. The corridor along which the plateau grows also narrows eastward, given the trend of the major faults bounding the area of active growth—i.e., the west-northwest trend of the sinistral Haiyuan and Ganshu fault zones and the northwest trend of the Qilian and Liupan Shan sinistral-oblique thrust belts along the northern margin of the plateau, and the northeast to east-northeast trend of the Longmen Shan thrust belt and the Qingchuan fault zone.

The orientations of the margins of this corridor may again be determined by the rheology of the bounding blocks, i.e., the South and North China Cratons. In this model, the northern edge of the topographically pronounced plateau margin in the Min Shan is due to contraction at the eastern termination of the Kunlun fault. Neogene–Holocene extension is governed by fault geometry (e.g., releasing bend interpretation of the Hanzhong Basin). Geodetic data suggest ≤3 mm/yr of active sinistral strike-slip faulting across the Qinling east of the area considered here (Heki et al., 1999; Chen et al., 2000). Thus the higher velocity of eastward displacement within the North China Craton part of the plateau than that of the South China Craton may be one reason for the dextral displacements documented in the southwestern Qinling. The termination of plateau growth on the North China Craton northwest of the Weihe graben might be responsible for the sinistral displacements along the eastern Qinling and farther east. In the plateau growth–backstop model, the eastward younging of the onset of rapid exhumation and the decrease in the amount of exhumation reflect the eastward propagation of shortening during plateau growth.

CONCLUSIONS

Cooling-history group 1 apatite fission-track samples indicate rapid cooling and local exhumation of ≥4 km during the Late Cretaceous, followed by a time of tectonic stability with retention of the samples at low temperatures throughout the Tertiary. These samples were taken along the northern Qinling and spatially overlap an area of Late Cretaceous–early Tertiary basin formation and strike-slip faulting. This exhumation, deformation, and basin-formation history agrees with the late Early Cretaceous to the late Late Cretaceous northwest-southeast compressional and northeast-southwest extensional stress field established previously for all of eastern China.

Cooling-history groups 2 and 3 fission-track samples were cooled to temperatures of partial track annealing (120–60 °C) and record continuous, slow to moderate cooling (~1.2 °C/m.y., locally up to 2.0 °C/m.y.) throughout the Qinling

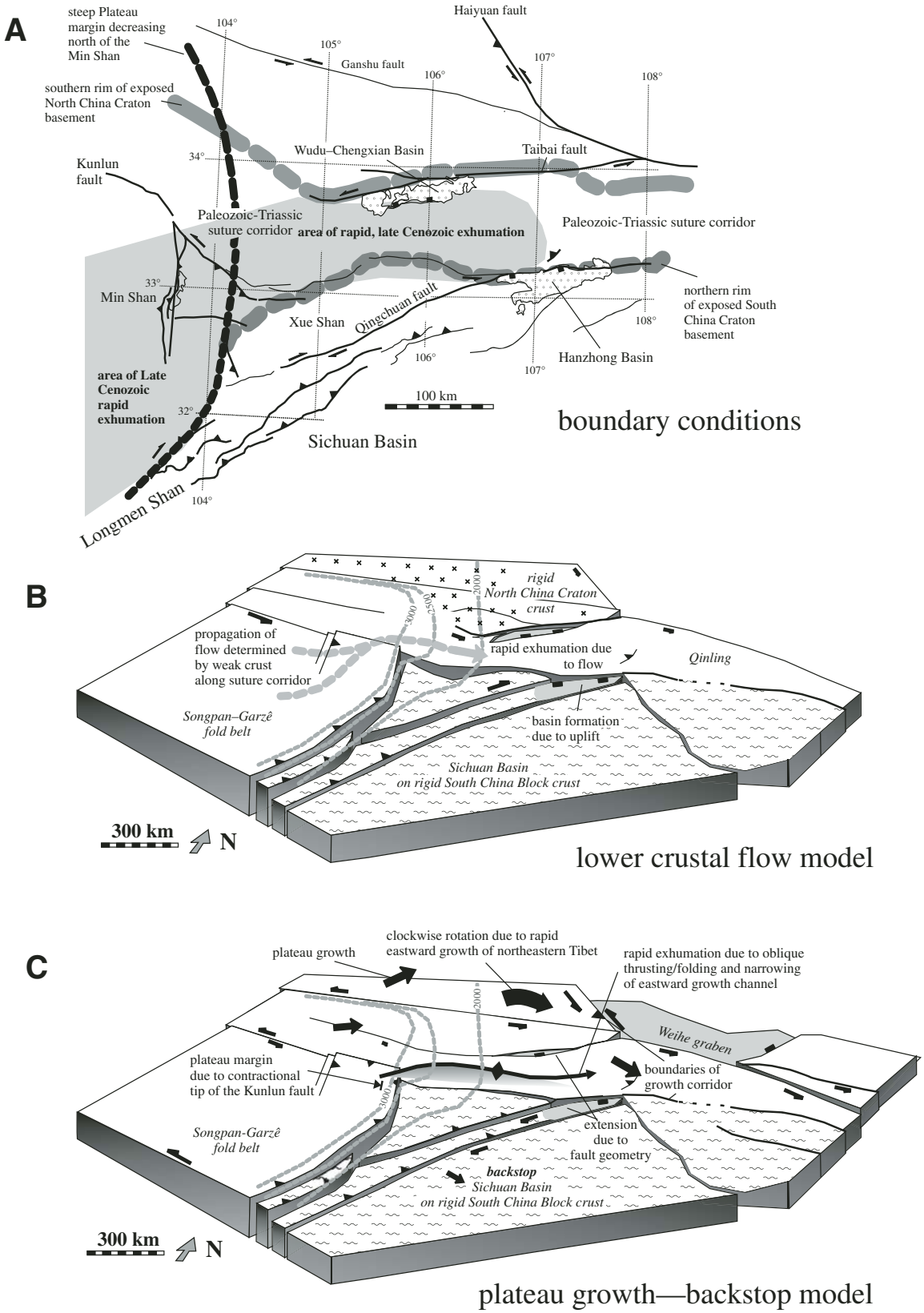

Figure 8. (A) Boundary conditions likely important in models describing the evolution of deformation and exhumation in the western Qinling. Shown are the locations of the southern and northern rims of exposed basement of the North and South China Cratons, major fault zones, the steep margin of the plateau, and the area of rapid, late Cenozoic exhumation defined by the fission-track data presented in this study (group 3 cooling histories; see text). (B, C) Illustrations of models discussed in text.

since at least 100–70 Ma; T[t]-path models indicate that slow to moderate cooling persisted throughout the Tertiary. The eastern Tibetan Plateau and the area north of the Kunlun fault zone show slow cooling of <3 °C/m.y. for the Cretaceous to the middle Miocene as well. The Qinling and Tibet data suggest that a stable region, characterized by insignificant exhumation and peneplanation, formed the low-amplitude, long-wavelength topography of the eastern Tibetan Plateau during the Late Cretaceous–Miocene.

Cooling-history group 3 fission-track samples from the southwestern Qinling signify rapid cooling and exhumation of 2–3 km at the very end of the thermal history; three samples from the southwestern Qinling suggest an onset at ca. 9–4 Ma. The cooling behavior of the Tibetan Plateau and the adjoining southwestern Qinling correspond. Cooling of the Tibetan Plateau began earlier, however, in the middle Miocene, and exhumation was stronger than in the Qinling; this independently constrains the onset of late-stage, rapid exhumation in the southwestern Qinling to be late Miocene or younger.

Two models fit the rapid, late-stage exhumation in the southwestern Qinling and relate it to the growth of the Tibetan Plateau. The lower crustal flow model suggests that where lower crustal flow encountered the strong basement of the Sichuan Basin, it was diverted northeastward along the rheologically "weak" crustal corridor along the Paleozoic–Mesozoic Qinling suture. Upper crustal responses of this flow include the sinistral strike-slip faults in the central western Qinling and the dextral strike-slip faults along the southern western Qinling. In this model, the eastward younging of the onset of rapid exhumation and the decrease in the amount of exhumation reflect the eastward propagation of lower crustal flow.

In the plateau growth–backstop model, rapid, late-stage exhumation in the southwestern Qinling results from oblique thrusting-folding along the northwestern margin of the South China Craton and the narrowing of the corridor along which the northeastern Tibetan Plateau is growing eastward; the rigid South China Craton acts as a backstop along which the shortening rate is diminished, and growth is channeled eastward. The eastward younging of the onset of rapid exhumation and the decrease in the amount of exhumation portrays the eastward propagation of shortening during plateau growth.

Regardless of which model is preferred, our study provides data that explain the geodetic difference between the velocities across the northeastern Tibetan Plateau and the Longmen Shan. Our study also documents horizontal and vertical material motion at the eastern growth tip of the Tibetan Plateau.

APPENDIX 1: APATITE FISSION-TRACK ANALYSIS

Sample Preparation, Irradiation, Age Calculation, and Standards

The apatite fractions were separated using heavy-liquid and electromagnetic techniques, and were mounted in epoxy, ground, and polished. The mounts were etched for 70 s in 2.5% HNO_3 at room temperature (6 samples) and 15 s in 23% HNO_3 at 25 °C (41 samples), covered with muscovite external detectors, and irradiated in channels 7 (epithermal/thermal fluence ratio: f = 116; epithermal neutron spectrum: $\varphi_e(E) \sim 1/E^{(1+\alpha)}$ with $\alpha = 0.072$; De Corte et al., 1986) and 8 (f = 163; $\alpha = 0.068$) of the Thetis reactor at the Institute for Nuclear Sciences of the University of Gent [Ghent] in Belgium. The muscovite external detectors were etched in 40% HF for 30 min at room temperature.

The thermal neutron fluence was calculated from the 411.8 keV gamma activity of Al-0.1%Au neutron fluence monitors (IRMM 530R), inserted at the top, middle, and bottom of the irradiation cans. Table 1 lists the thermal neutron fluences; their combined systematic and statistical error is ~2% (Van den haute et al., 1988; Jonckheere, 1995). To check the accuracy of the age determinations with the independent method (ϕ method; Jonckheere, 2003a), all samples except Q113 were also dated with the Z and ζ methods (Hurford and Green, 1982, 1983). Two mounts of Fish Canyon and Durango age standards and Limberg t3 tuff apatites (a proposed age standard; Rahn et al., 2001) were included in each irradiation. These were prepared in the same manner as the samples (Jonckheere and Wagner, 2000b) with two exceptions: (1) ~1-mm-thick slices, cut parallel to the prismatic faces of a single crystal of Durango apatite, were used instead of shards obtained by crushing. This ensures that the track counts in the age standard were performed on the same surfaces that were selected for the fission-track counts in the samples; (2) millimeter-sized shards of the Corning CN5 or IRMM 540R standard uranium glasses were embedded together with the age standards. This ensures a minimum separation between the standard glasses and apatite age standards.

The ζ values in Table 1 show that there exists a significant difference between the mean ζ values for the four analysts ($\zeta_{CN5[1]} = 341 \pm 4$ a cm^2, $\zeta_{CN5[2]} = 369 \pm 7$ a cm^2, $\zeta_{IRMM[1]} = 282 \pm 5$ a cm^2, $\zeta_{IRMM[3]} = 287 \pm 19$ a cm^2, and $\zeta_{IRMM[4]} = 267 \pm 7$ a cm^2), which is ascribed to different track-identification criteria. However, all analysts obtained ζ ages for all samples that are in agreement with their independent fission-track ages (ϕ ages) and Z ages (Table 1; Fig. A1A). Their different track identification criteria thus did not introduce systematic errors. The relatively high difference between the ϕ ages and the Z and ζ ages of the samples dated by analyst [3] is explained by the large scatter of the single ζ values and the resulting error ($1\sigma = 19$ a cm^2) of this analyst.

The independent fission-track ages were calculated using the equation $t = 1/\lambda_\alpha \, ln \, [(\lambda_\alpha/\lambda_F) \, G \, Q \, R \, (\rho_s/\rho_i) \, I \, \phi \, \sigma_0 + 1]$ with an alpha-decay constant of ^{238}U, $\lambda_\alpha = 1.551 \, 10^{-10}$ a^{-1} (Jaffey et al., 1971); a fission-decay constant of ^{238}U, $\lambda_F = 8.5 \, 10^{-17}$ a^{-1} (Holden and Hoffman, 2000); a geometry factor, G = 0.5; an isotopic ratio, $^{235}U/^{238}U$, $I = 7.253 \, 10^{-3}$ (Cowan and Adler, 1976); ϕ, a subcadmium neutron fluence in the Høgdahl convention; an effective 2200 m/s cross section for the $^{235}U(n,f)$ reaction, $\sigma_0 = 586 \, 10^{-24}$ cm^2 (Holden and Holden, 1989). The *Q* factor represents the ratio of the track counting efficiencies in a muscovite external detector and an apatite internal surface. *Q* depends on the track-identification criteria and is a personal calibration factor in the same way as ζ. *R* represents the deficit between the latent and etchable track length in the mineral and the external detector. The combined *QR* factor was determined from the ratio of induced track densities in internal apatite surfaces and co-irradiated external detectors (Jonckheere, 1995; Enkelmann and Jonckheere, 2003). The *QR* values of the four analysts ($QR_{[1]} = 1.20 \pm 0.01$, $QR_{[2]} = 1.20 \pm 0.01$, $QR_{[3]} = 1.15 \pm 0.06$, and $QR_{[4]} = 1.19 \pm 0.02$) are again different as a result of different track-identification criteria. The dissimilar *QR* and ζ factors of the analysts reveal the magnitude of the effect of track-identification criteria in fission-track counting. The consistency of the ϕ, Z, and ζ ages, on the other hand, shows that they are adequately dealt with in both dating methods.

Track Counting

Track counting was performed on prismatic apatite surfaces with a Zeiss Axioplan microscope at a nominal magnification of 500 using transmitted light. The muscovite external detectors were repositioned, track-side down, on the apatite mounts in the same position as during irradiation. Fossil tracks were counted by focusing on the apatite surface through the muscovite detector; induced tracks were counted by focusing on the underside of the external detector without moving the microscope stage (Jonckheere et al., 2003). Whenever possible, at least 20 grains were dated; all suitable grains were counted in samples that contained <20 grains.

Track-Length Measurements

Track-length measurements were performed at a nominal magnification of 1500 using the Zeiss Axioplan microscope equipped with the Autoscan system (Autoscan Systems Pty. Ltd.). All suitable confined tracks parallel to the prismatic surfaces were measured. Only TINTs (Track IN Track) were registered. Separate mounts were prepared for 14 samples (Q1, Q3, Q4, Q8, Q31, Q37, Q43, Q55, Q65, Q67, Q69, Q113, Q123, Q127) that yielded sufficient apatite for additional track-length measurements. These mounts were irradiated with heavy ions at GSI Darmstadt to increase the number of etchable confined tracks.

Thermal History Modeling

Dpar (the arithmetic mean maximum diameter of fission-track etch figures, measured parallel to the c-axis; Burtner et al., 1994, Donelick, 1993) was measured for samples with more than 25 confined tracks. The Dpar values range between 1.5 and 2.3 μm, and neither correlate with the fission-track age (Fig. A1B) nor with the mean track length (Fig. A1C). That is not surprising, as most apatite compositions are close to that of Durango ($|Cl-1| \approx 0.88$; Dpar = 1.83 μm), and variations within the range $0.75 < |Cl-1| < 1.0$ (Dpar 1.5–3.0 μm) have no measurable effect or, at most, only a moderate effect on the annealing kinetics (Ketcham et al., 1999; Fig. 7A and its discussion). The effect of apatite composition on the T[t] paths is to shift the paleotemperature estimates up or down by ~20 °C in the high-temperature region, and much less at lower temperatures. The compositional effect is less important than the one from the number and positions of modeling constraints and statistical uncertainties resulting from the confined track-lengths spread. For

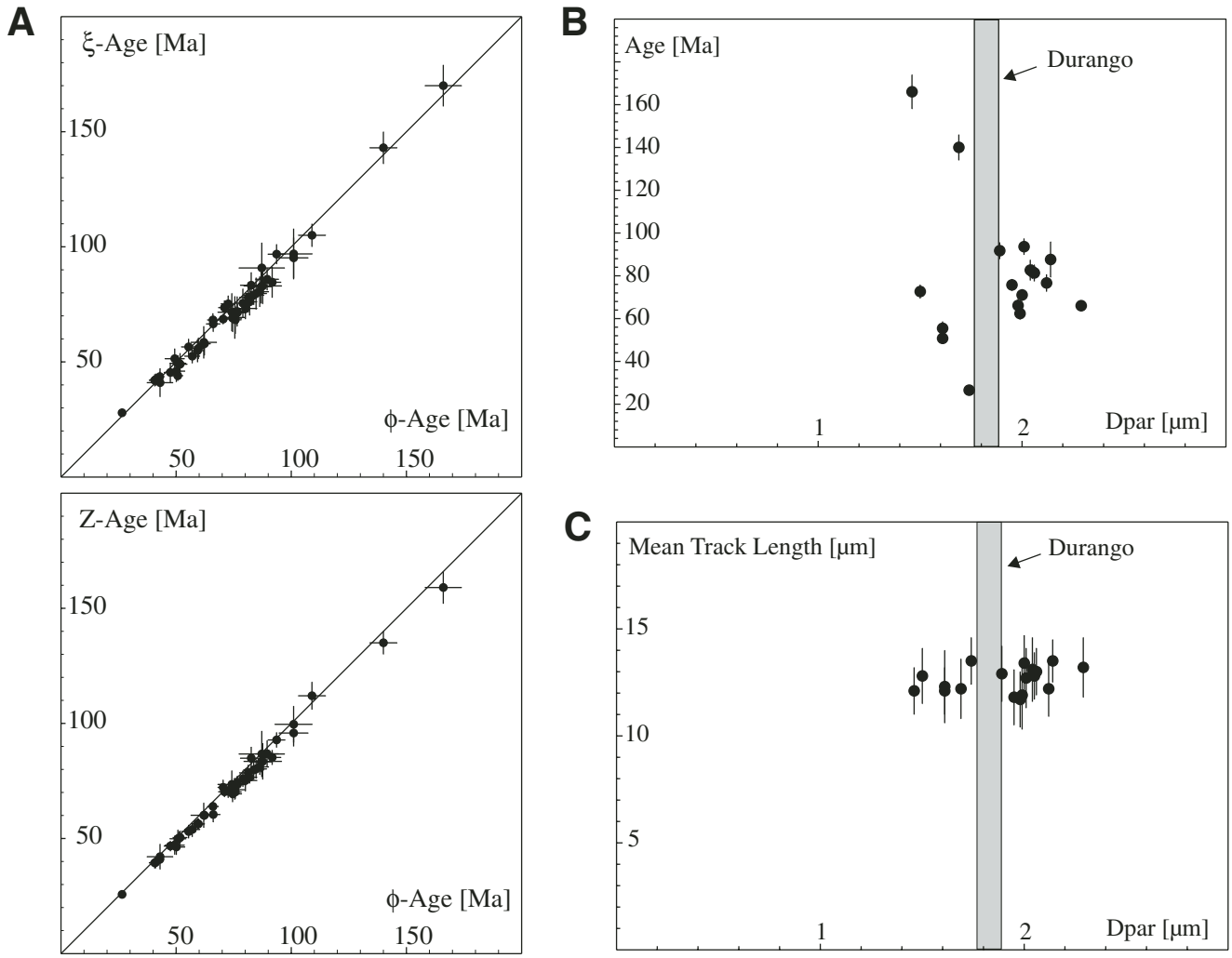

Figure A1. (A) The ζ and Z apatite fission-track ages of samples analyzed in this study, plotted against their independent ages (ϕ age). The good agreement provides a strong argument that the ages are accurate. The error bars represent 1σ statistical errors. The kinetic parameter Dpar is plotted against the fission-track age (B) and against the mean track length (C). For reference, the Dpar value of the Durango apatite is shown as the gray bar.

these reasons, we selected the annealing equations of Laslett et al. (1987), which we believe approximately describe the annealing kinetics of our samples. Moreover, our interpretations are not based on the exact temperature predicted by the modeling results but on the sample age and the shape of the track-length distribution, the relationship of neighboring samples, and geological structures.

The thermal histories were modeled with AFTSolve 1.1.3 (Ketcham et al., 2000). As a rule, 10,000 candidate T[t] paths were generated by a Monte Carlo process. Much longer test runs confirmed that the solutions remained stable after 10,000 iterations. The Monte Carlo procedure was preferred, as more efficient search algorithms are not well enough understood to exclude the possibility that they converge toward a local maximum. No minimum or maximum heating or cooling rates were set, because no such limits are imposed by independent geological information. The segments that connect the nodes defining each T[t] path were not subdivided. This has the effect that the number of degrees of freedom of the T[t] path is limited to $2n$, where n represents the number of free nodes. Because the number of free nodes is determined by the number of user-entered constraints, this procedure enabled us to discriminate between different T[t] solutions by repeated modeling of a single sample with well-considered changes of the number and position of the constraints. This procedure showed that the selection of constraints has an important effect on the resulting T[t] paths. To keep track of how the number and position of constraints affect the modeling results, we consistently used a minimum number of constraints and modeled each sample several tens of times, gradually shifting their position. In this study, we have set a pair of initial and a pair of final constraints.

Estimation of Onset of Rapid Cooling in the Southwestern Qinling

With their symmetric track-length distributions, cooling-history group 3 samples indicate that prolonged slow cooling within the upper part of the PAZ (90–60 °C) was followed by rapid cooling to temperatures below 60 °C (low temperature zone: LTZ) at the end of the thermal history. Owing to the artifact, it is impossible to estimate the onset of rapid cooling using T[t]-path modeling (as previously explained). Here, we use the linear relationship between the fission-track age and the number of tracks to calculate the time interval that is represented by a certain track-length interval. The number of lengths of the track-length distribution that represent the PAZ and LTZ corresponds to the time intervals during which the samples stayed in the PAZ and the LTZ, respectively (Fig. 6). For the group 3 samples, we suggested that the time these samples spent in the LTZ equals the time since the onset of rapid cooling.

Figure 6 shows the track-length distribution of sample Q65 with 185 measured tracks *(N)* and an apparent fission-track age *(t)* of 62.3 Ma. The number of tracks (n_i) with a certain length (l_i) represent a certain time interval (Δt_i) that is calculated according to equation 1:

$$\Delta t_i = \frac{n_i}{N} t \,. \quad (1)$$

TABLE A1. CORRECTION OF TRACK-LENGTH DISTRIBUTION AND ESTIMATION OF ONSET OF FAST EXHUMATION

Sample	N	t (Ma)	N_0	t_0 (Ma)	$n_0 \geq 14$	$n_0 \leq 14$	t_{PAZ} (Ma)	t_{LTZ} (Ma)
Q65	185	62.3	258	87.0	17	241	81.1	5.9
Q67	173	76.6	234	103.5	20	214	94.6	8.9
Q69	207	75.7	290	105.9	12	278	101.4	4.5

Note: N—number of measured tracks; t—apparent fission-track age; N_0—corrected number of tracks; t_0—corrected fission-track age; n_0—number of tracks for certain length; t_{PAZ}—residence time in the partial annealing zone; t_{LTZ}—residence time in the total stability zone.

The linear relationship between the track length and the track density causes the length distribution to be biased toward short tracks (Green, 1988), and thus the number of tracks in each interval of the distribution has to be corrected according to equation 2,

$$n_{0i} = \frac{l_0}{l_i} n_i , \quad (2)$$

with n_{0i} the corrected number of tracks, with length, l_i. The etchable length of induced tracks (16.3 µm; e.g., Green et al., 1986; Gleadow et al., 1986) is used as the initial track length (l_0). After correcting the number of tracks, the corrected time span (Δt_{0i}) is calculated for each length interval according to equation 3:

$$\Delta t_{0i} = \frac{n_{0i}}{n_i} \Delta t_i . \quad (3)$$

The sum of all Δt_{0i} is the corrected fission-track age (t_0) and indicates the time since the formation of the oldest track.

Our estimate of the residence time of the group 3 samples in the LTZ is based on the corrected length distribution (Fig. 6 and Table A1). It is accepted that the mean length of tracks that formed in the LTZ over geologic time is reduced relative to the induced track length and ranges between ~14 to 15 µm (Green 1980, 1981, 1988; Watt et al., 1984; Watt and Durrani, 1985; Gleadow et al., 1986; Green et al., 1986; Donelick, 1991; Donelick et al., 1990; mean track length of age standards: Durango, 14.5 µm; Fish Canyon Tuff, 14.9 µm; Mount Dromedary, 14.1 µm; Enkelmann et al., 2005). We divided the corrected length distribution at 14 µm to separate the tracks formed in the PAZ (tracks <14 µm) from tracks formed in the LTZ (tracks ≥14 µm). We also assumed that the number of tracks >14 µm that belong to the PAZ track-length distribution is equal to the number of tracks <14 µm that belong to the LTZ track-length distribution. The residence time in the PAZ (t_{PAZ}) and the LTZ (t_{LTZ}) is calculated following equations 4 and 5:

$$t_{PAZ} = \sum_{i \leq 14} \Delta t_{0i} ; \quad (4)$$

$$t_{LTZ} = \sum_{i \leq 14} \Delta t_{0i} . \quad (5)$$

This approach only approximates the age of onset of rapid cooling, as the obtained number is strongly sensitive to the length at which the distribution is divided, and the calculation depends on the assumption that the PAZ and LTZ track-length distributions contribute approximately equally to the number of tracks where they superimpose. We applied this approach to samples Q65, Q67, and Q69 (N = 173–207) and estimated that the onset of fast cooling was ca. 9–4 Ma (Table A1).

APPENDIX 2: FAULT-SLIP ANALYSIS

Fault-slip data were collected from outcrops of known or assumed stratigraphic position. Each station is an outcrop of up to quarry size with uniform lithology. The sense of slip along the faults was deduced from kinematic indicators—e.g., offset markers, fibrous minerals grown behind fault steps, Riedel shears, tension gashes, and the like (e.g., Petit et al., 1983). Because errors in slip-sense determination may have severe effects on the calculation of principal stress axes, a confidence level was assigned to each slip-sense datum. These levels are recorded in the style of arrowheads, expressing the slip direction of the hanging wall block in the fault-slip data diagrams, thus allowing judgment of the quality of the database. The surface morphology of the slickensides and the fault size, classified qualitatively by estimating the displacement and the lateral extent of the fault, were recorded. The aim was to identify first-order faults and to enable a comparison of faults measured in outcrops with those inferred from mapping. Multiple slip was recorded, and the relative chronology was used for separation of heterogeneous raw-data fault sets into subsets. Overprinting relationships, such as consistent fault superposition, overgrowths of differently oriented fibers, or fibers with changing growth direction, guided the assignment of the subsets to relative age groups.

We used the computer-program package of Sperner et al. (1993) for fault-slip analysis to calculate the orientation of principal stress axes and the reduced stress tensors (e.g., Angelier, 1994). Out of this package, we obtained stress axes by the "pressure-tension (P-B-T) axes" method (Turner, 1953) and calculated stress tensors by the "numerical dynamic analysis" of Spang (1972). In addition to stress orientation, the computation of the reduced stress tensor determines the ratio, R, which expresses the relationship between the magnitudes of the principal stresses. Extreme values of R correspond to stress ellipsoids with $\sigma_2 = \sigma_3$ ($R = 0$) or $\sigma_1 = \sigma_2$ ($R = 1$). The quality and quantity of field data determined the selection of the method used for calculation. The P-B-T axes method was used with scarce data and where insufficient time was available in the field for careful analysis of fault and striae characteristics.

ACKNOWLEDGMENTS

This study was funded by grants Ra 442/19 and 20 from the Deutsche Forschungsgemeinschaft. R. Ketcham and R. Donelick supplied AFTSolve free of charge. D. Arne provided detailed track-length data from his Tibetan samples. Ch. Trautmann made the heavy ion irradiation at the GSI in Darmstadt possible. The topographic maps and profiles in this paper were generated using the public domain Generic Mapping Tools (GMT) software (Wessel and Smith, 1995). We thank A. Görner for help with compiling the topographic database. Finally, we thank Associate Editor E. Kirby, C.J.L. Wilson, and an anonymous reviewer for constructive reviews.

REFERENCES CITED

Angelier, J., 1994, Fault-slip analysis and paleostress reconstruction, *in* Hancock, P.L., ed., Continental deformation: Tarrytown, New York, Pergamon Press, p. 53–100.

Arne, D., Worley, B., Wilson, C., Chen, S.F., Foster, D., Lou, Z., Liu, S., and Dirks, P.H.G.M., 1997, Differential exhumation in response to episodic thrusting along the eastern margin of the Tibet Plateau: Tectonophysics, v. 280, p. 239–256, doi: 10.1016/S0040-1951(97)00040-1.

Bellier, O., Mercier, J.L., Vergély, P., Long, C., and Ning, C., 1988, Evolution sédimentaire et tectonique du graben cenozoique de la Wei He (Province du Shaanxi, Chine du Nord): Bulletin de la Société Géologique de France, v. 6, p. 979–994.

Bellier, O., Vergély, P., Mercier, J.L., Ning, C., Deng, N., Yi, M., and Long, C., 1991, Analyse tectonique et sédimentaire dans les monts Li Shan (province du Shaanxi, Chine du Nord): datation des régimes tectoniques extensifs dans le graben de la Wei He: Bulletin de la Société Géologique de France, v. 162, p. 101–112.

Belton, D.X., Kohn, B.P., and Gleadow, A.J.W., 2004, Extracting track age spectra from raw FT data—A method of establishing the "cooling onset age" and "event timing" in natural samples: Amsterdam, International Conference of Fission Track Analysis, DVL-06-P.

BGMRSX, 1989, Regional geology of Shanxi Province, Beijing: Beijing, Geological Publishing House, 689 p.

BGMRSX, 1991, Geological Map of Qinling-Daba Mountains and adjacent regions of the People's Republic of China: Beijing, Geological Publishing House, scale 1:1,000,000, 1 sheet.

Burchfiel, B.C., Chen, Z., Liu, Y., and Royden, L.H., 1995, Tectonics of the Longmen Shan and adjacent regions, central China: International Geology Review, v. 37, p. 661–735.

Burtner, R.L., Nigrini, A., and Donelik, R.A., 1994, Thermochronology of Lower Cretaceous source rocks in the Idaho-Wyoming Thrust Belt: American Association of Petroleum Geologists Bulletin, v. 78, p. 1613–1636.

Chen, S.F., and Wilson, C.J.L., 1996, Emplacement of the Longmen Shan Thrust-Nappe Belt along the eastern margin of the Tibetan Plateau: Journal of Structural Geology, v. 18, p. 413–430, doi: 10.1016/0191-8141(95)00096-V.

Chen, S.F., Wilson, C.J.L., and Worley, B.A., 1995, Tectonic transition from the Songpan-Ganze Fold Belt to the Sichuan Basin, south-western China: Basin Research, v. 7, p. 235–253.

Chen, W., Li, Q., Li, D., and Wang, X., 1990, Geochronological implications of K/Ar isotope system of fault gouge: A preliminary study: Physics and Chemistry of the Earth, v. 17, p. 17–23, doi: 10.1016/0079-1946(89)90004-9.

Chen, Z.K., Zhao, C., Yin, A., Li, Y., Jackson, D.D., Fang, P., and Dong, D., 2000, Contemporary crustal deformation in East Asia constrained by Global Positioning System measurements: Journal of Geophysical Research, v. 105, p. 5721–5734, doi: 10.1029/1999JB900391.

Chen, Z., Burchfiel, B.C., Liu, Y., King, R.W., Royden, L.H., Tang, W., Wang, E., Zhao, J., and Zhang, X., 2000, Global Positioning System measurements from eastern Tibet and their implications for India/Eurasia intercontinental deformation: Journal of Geophysical Research, B, Solid Earth and Planets, v. 105, p. 16,215–16,227, doi: 10.1029/2000JB900092.

Clark, M.K., and Royden, L.H., 2000, Topographic ooze: Building the eastern margin of Tibet by lower crustal flow: Geology, v. 28, p. 703–706, doi: 10.1130/0091-7613(2000)028<1143:OAOMCL>2.3.CO;2.

Clark, M.K., Schoenbohm, L.M., Royden, L.H., Whipple, K.X., Burchfiel, B.C., Zhang, X., Tang, W., Wang, E., Chen, L., 2004, Surface uplift, tectonics, and

erosion of eastern Tibet from large-scale drainage patterns: Tectonics, v. 23, TC1006, p. 1–20, doi:10.1029/2002TC001402.

Clark, M.K., House, M.A., Royden, L.H., Whipple, K.X., Burchfiel, B.C., Zhang, X., and Tang, W., 2005, Late Cenozoic uplift of southeastern Tibet: Geology, v. 33, p. 525–528, doi: 10.1130/G21265.1.

Cowan, G.A., and Adler, H.H., 1976, The variability of the natural abundance of 235U: Geochimica et Cosmochimica Acta, v. 40, p. 1487–1490, doi: 10.1016/0016-7037(76)90087-9.

De Corte, F., Moens, L., Jovannovic, S., Simonits, A., and Dewispelaere, A., 1986, Applicability of the $1/E^{1+\alpha}$ epithermal spectrum representation and the effective resonance energy in NAA: Radiaoanalytical Nuclear Chemistry Articles, v. 102, p. 37–57, doi: 10.1007/BF02037948.

Dirks, P.H.G.M., Wilson, C.J.L., Chen, S., Luo, Z.L., and Liu, S., 1994, Tectonic evolution of the NE margin of the Tibetan Plateau; evidence from the central Longmen Mountains, Sichuan Province, China: Journal of Southeast Asian Earth Sciences, v. 9, p. 181–192, doi: 10.1016/0743-9547(94)90074-4.

Donelick, R.A., 1991, Crystallographic orientation dependence of mean etchable fission-track length in apatite: An empirical model and experimental observations: American Mineralogist, v. 76, p. 83–91.

Donelick, R.A., 1993, A method of fission-track analysis utilizing bulk chemical etching of apatite: U.S. Patent No. 5,267,274.

Donelick, R.A., Roden, M.K., Mooers, J.D., Carpenter, B.S., and Miller, D.S., 1990, Etchable length reduction of induced fission tracks in apatite at room temperature (≈23°C): Crystallographic orientation effects and 'initial' mean lengths: Nuclear Tracks and Radiation Measurements, v. 17, p. 261–265, doi: 10.1016/1359-0189(90)90044-X.

Enkelmann, E., and Jonckheere, R., 2003, Correction factors for systematic errors related to the track counts in fission-track dating with the external detector method: Radiation Measurements, v. 36, p. 351–356, doi: 10.1016/S1350-4487(03)00150-1.

Enkelmann, E., Ratschbacher, L., and Jonckheere, R., 2004, Cenozoic tectonics of the easternmost Tibetan Plateau: Constraints from fission-track geochronology, American Geophysical Union Fall Meeting: Eos (Transactions of the American Geophysical Union), v. 85, T31B-1298.

Enkelmann, E., Jonckheere, R., and Wauschkuhn, B., 2005, Independent fission-track ages (ϕ-ages) of accepted and proposed apatite age standards and a comparison of ϕ-, Z-, ζ- and ζ_0-ages: Implications for method calibration: Chemical Geology, v. 222, p. 232–248, doi: 10.1016/j.chemgeo.2005.07.009.

Fielding, E., Isacks, B.L., Barazangi, M., and Duncan, C., 1994, How flat is Tibet?: Geology, v. 22, p. 163–167, doi: 10.1130/0091-7613(1994)022<0163:HFIT>2.3.CO;2.

Gaudemer, Y., Tapponnier, P., Meyer, B., Peltzer, G., Guo, S., Chen, Z., Dai, H., and Cifuentes, I., 1995, Partitioning crustal slip between linked, active faults in the eastern Qilian Shan, and evidence for a major seismic gap, the "Tianzhu Gap", on the western Haiyuan Fault, Gansu (China): Geophysical Journal International, v. 120, p. 599–645.

Gleadow, A.J.W., Duddy, I.R., Green, P.F., and Hegarty, K.A., 1986, Fission track length in the apatite annealing zone and the interpretation of mixed ages: Earth and Planetary Science Letters, v. 78, p. 245–254, doi: 10.1016/0012-821X(86)90065-8.

Green, P.F., 1980, On the cause of the shortening of spontaneous fission tracks in certain minerals: Nuclear Tracks, v. 4, p. 91–100, doi: 10.1016/0191-278X(80)90018-9.

Green, P.F., 1981, 'Track in track' length measurements in annealed apatites: Nuclear Tracks, v. 5, p. 121–128, doi: 10.1016/0191-278X(81)90034-2.

Green, P.F., 1986, On the thermo-tectonic evolution of Northern England: Evidence from fission-track analysis: Geological Magazine, v. 123, p. 493–506.

Green, P.F., 1988, The relationship between track shortening and fission-track age reduction in apatite: Combined influences of inherent instability, annealing anisotropy, length bias and system calibration: Earth and Planetary Science Letters, v. 89, p. 335–352, doi: 10.1016/0012-821X(88)90121-5.

Green, P.F., Duddy, I.R., Gleadow, A.J.W., Tingate, P.R., and Laslett, G.M., 1986, Thermal annealing of fission tracks in apatite 1, A qualitative description: Chemical Geology, v. 59, p. 237–253, doi: 10.1016/0009-2541(86)90048-3.

Grimmer, J.C., Jonckheere, R., Enkelmann, E., Ratschbacher, L., Hacker, B.R., Blythe, A., Wagner, G.A., Liu, S., and Dong, S., 2002, Cretaceous–Tertiary history of the southern Tan-Lu fault zone: Apatite fission-track and structural constraints from the Dabie Shan: Tectonophysics, v. 359, p. 225–253, doi: 10.1016/S0040-1951(02)00513-9.

Hacker, B.R., Ratschbacher, L., Webb, L., McWilliams, M.O., Ireland, T., Calvert, A., Dong, S., Wenk, H.-R., and Chateigner, D., 2000, Exhumation of ultrahigh-pressure continental crust in east central China: Late Triassic–Early Jurassic tectonic unroofing: Journal of Geophysical Research, v. 105, p. 13,339–13,364, doi: 10.1029/2000JB900039.

Harrowfield, M.J., and Wilson, C.J.L., 2005, Indosinian deformation of the Songpan Garzê fold belt, northeast Tibetan Plateau: Journal of Structural Geology, v. 27, p. 101–117, doi: 10.1016/j.jsg.2004.06.010.

Heki, K., Miyazaki, S., Takahashi, H., Kasahara, M., Kimata, F., Miura, S., Vasilenko, N.F., Ivashchenko, A., and An, K.-D., 1999, The Amurian Plate motion and current plate kinematics in eastern Asia: Journal of Geophysical Research, B, Solid Earth and Planets, v. 104, p. 29,147–29,155, doi: 10.1029/1999JB900295.

Holden, N.E., and Hoffman, D.C., 2000, Spontaneous fission half-lives for ground-state nuclides: Pure and Applied Chemistry, v. 72, p. 1525–1562.

Holden, N.E., and Holden, K.A., 1989, Reexamination of 2200 m/s cross section experiments for neutron capture and fission standards: Pure and Applied Chemistry, v. 61, p. 1505–1510.

Hurford, A.J., and Green, P.F., 1982, A user's guide to fission track dating calibration: Earth and Planetary Science Letters, v. 59, p. 343–354, doi: 10.1016/0012-821X(82)90136-4.

Hurford, A.J., and Green, P.F., 1983, The zeta calibration of fission track dating: Isotope Geosciences, v. 1, p. 285–317.

Jaffey, A.H., Flynn, K.F., Glemndenin, L.E., Bentley, W.C., and Essling, A.M., 1971, Precision measurements of the half-lives and specific activities of 235U and 238U: Physical Review, v. C4, p. 1889–1906.

Jonckheere, R., 1995, Absolute age determination of apatite based on uranium fission-tracks: A methodical investigation [Ph.D. thesis]: Belgium, University of Gent, 504 p.

Jonckheere, R., 2003a, On the densities of etchable fission tracks in a mineral and co-irradiated external detector with reference to fission-track dating of minerals: Chemical Geology, v. 200, p. 41–58, doi: 10.1016/S0009-2541(03)00116-5.

Jonckheere, R., 2003b, On the methodical problems in estimating geological temperature and time from measurements of fission tracks in apatite: Radiation Measurements, v. 36, p. 43–55, doi: 10.1016/S1350-4487(03)00096-9.

Jonckheere, R., and Wagner, G.A., 2000a, The KTB apatite fission-track profile: The significance of bore-hole data in fission-track analysis: Geological Society of Australia Abstracts, v. 58, p. 193–194.

Jonckheere, R., and Wagner, G.A., 2000b, A non-standard procedure for the analysis of external-detector samples introduced at the Heidelberg fission-track lab: Geological Society of Australia Abstracts, v. 58, p. 191–192.

Jonckheere, R., Ratschbacher, L., and Wagner, G.A., 2003, A repositioning technique for counting induced fission tracks in muscovite external detectors in a single-grain dating of minerals with low and inhomogeneous uranium concentrations: Radiation Measurements, v. 37, p. 217–219, doi: 10.1016/S1350-4487(03)00029-5.

Jones, L.M., Han, W., Hauksson, E., Jin, A., Zhang, Y., and Luo, Z., 1984, Focal mechanisms and aftershock locations of the Songpan Earthquakes of August 1976 in Sichuan, China: Journal of Geophysical Research, B, Solid Earth and Planets, v. 89, p. 7697–7707.

Ketcham, R.A., Donelick, R.A., and Carlson, W.D., 1999, Variability of apatite fission-track annealing kinetics: III, Extrapolation to geological time scales: American Mineralogist, v. 84, p. 1235–1255.

Ketcham, R.A., Donelick, R.A., and Donelick, M.B., 2000, AFTSolve: A program for multikinetic modeling of apatite fission-track data: Geological Materials Research, v. 2, p. 1–32.

King, R.W., Shen, F., Burchfiel, B.C., Royden, L.H., Wang, E., Chen, Z., Liu, Y., Zhang, X., Zhao, J., and Li, Y., 1997, Geodetic measurements of crustal motion in Southwest China: Geology, v. 25, p. 179–182, doi: 10.1130/0091-7613(1997)025<0179:GMOCMI>2.3.CO;2.

Kirby, E., Whipple, K.X., Tang, W., Burchfiel, B.C., and Chen, Z., 2000, Neotectonics along the eastern margin of the Tibetan Plateau; inferences from bedrock river incision patterns: Earth Science Frontiers, v. 7, p. 281–282.

Kirby, E., Reiners, P.W., Krol, M.A., Whipple, K.X., Hodges, K.V., Farley, K.A., Tang, W., and Chen, Z., 2002, Late Cenozoic evolution of the eastern margin of the Tibetan Plateau: Inferences from 40Ar/39Ar and (U-Th)/He thermochronology: Tectonics, v. 21, TC1001, p. 1–20, doi: 10.1029/2000TC001246.

Kirby, E., Whipple, K.X., Tang, W., and Chen, Z., 2003, Distribution of active rock uplift along the eastern margin of the Tibetan Plateau: Inferences from bedrock channel longitudinal profiles: Journal of Geophysical Research, B, Solid Earth and Planets, v. 108, no. B4, p. 16-1–16-24.

Laslett, G.M., Green, P.F., Duddy, I.R., and Gleadow, A.J.W., 1987, Thermal annealing of fission-tracks in apatite, 2, A quantitative analysis: Chemical Geology, v. 65, p. 1–13, doi: 10.1016/0009-2541(87)90189-6.

Lasserre, C., Morel, P.H., Gaudemer, Y., Tapponnier, P., Ryerson, F.J., King, G.C.P., Metivier, F., Kasser, M., Kashgarian, M., Liu, B., Lu, T., and Yuan, D., 1999, Postglacial left slip rate and past occurrence of M≥8 earthquakes on the western Haiyuan fault, Gansu, China: Journal of Geophysical Research, B, Solid Earth and Planets, v. 104, p. 17,633–17,652, doi: 10.1029/1998JB900082.

Mattauer, M., Matte, Ph., Malavieille, J., Tapponnier, P., Maluski, H., Qin, X.Z., Lun, L.Y., and Qin, T.Y., 1985, Tectonics of the Qinling Belt: Build-up and evolution of eastern Asia: Nature, v. 317, p. 496–500, doi: 10.1038/317496a0.

Mattauer, M., Malavieille, J., Calassou, S., Lancelot, J., Roger, F., Hao, Z., Xu, Z., and Hou, L., 1992, The Songpan-Garze Triassic belt of western Sichuan and eastern Tibet; a decollement–fold belt on passive margin: Paris, Comptes Rendus de L'Academie des Sciences, v. 314, p. 619–626.

Metivier, F., Gaudemer, Y., Tapponnier, P., and Meyer, B., 1998, Northeastward growth of the Tibet Plateau deduced from balanced reconstruction of two depositional areas; the Qaidam and Hexi Corridor basins, China: Tectonics, v. 17, p. 823–842, doi: 10.1029/98TC02764.

Meyer, B., Tapponnier, T., Bourjot, L., Metivier, F., Gaudemer, Y., Peltzer, G., Guo, S., and Chen, Z., 1998, Crustal thickening in Gansu-Qinghai, lithospheric mantle subduction, and oblique, strike-slip controlled growth of the Tibet Plateau: Geophysical Journal International, v. 135, p. 1–47, doi: 10.1046/j.1365-246X.1998.00567.x.

Nie, S., Yin, A., Rowley, D.B., and Jin, Y., 1994, Exhumation of the Dabie Shan ultra-high pressure rocks and accumulation of the Songpan-Ganzi flysch sequence, central China: Geology, v. 22, p. 999–1002, doi: 10.1130/0091-7613(1994)022<0999:EOTDSU>2.3.CO;2.

Peltzer, G., Tapponnier, P., Zhitao, Z., and Qin, X.Z., 1985, Neogene and Quaternary faulting in and along the Qinling Shan: Nature, v. 317, p. 500–505, doi: 10.1038/317500a0.

Petit, J.P., Proust, F., and Tapponnier, P., 1983, Criteria of the movement orientation of fault mirrors in non-calcareous rocks: Bulletin de la Société Géologique de France, v. 25, p. 589–608.

Rahn, M., Kraml, M., and Pik, R., 2001, A new apatite and titanite standard for fission-track and (U-Th)/He dating: On Track, v. 22, p. 9.

Ratschbacher, L., Frisch, W., Chen, C., and Pan, G., 1996, Cenozoic deformation, rotation, and stress patterns in eastern Tibet and western Sichuan, China, *in* Yin, A., et al., eds., The tectonic evolution of Asia: Cambridge, UK, Cambridge University Press, p. 227–249.

Ratschbacher, L., Hacker, B.R., Webb, L.E., McWilliams, M., Ireland, T., Dong, S., Calvert, A., Chateigner, D., and Wenk, H.-R., 2000, Exhumation of the ultrahigh-pressure continental crust in east China: Cretaceous and Cenozoic unroofing and the Tan-Lu fault: Journal of Geophysical Research, v. 105, p. 303–338, doi: 10.1029/2000JB900040.

Ratschbacher, L., Hacker, B.R., Calvert, A., Webb, L.E., Grimmer, J.C., McWilliams, M.O., Ireland, T., Dong, S., and Hu, J., 2003, Tectonics of the Qinling (Central China): Tectonostratigraphy, geochronology and deformation history: Tectonophysics, v. 366, p. 1–53, doi: 10.1016/S0040-1951(03)00053-2.

Reiners, P.W., Zhou, Z., Ehlers, T.A., Xu, C., Brandon, M.T., Donelick, R.A., and Nicolescu, S., 2003, Post-orogenic evolution of the Dabie Shan, eastern China, from (U-Th)/He and fission-track thermochronology: American Journal of Science, v. 303, p. 489–518.

Roger, F., Malavielle, J., Leloup, Ph.H., Calassou, S., and Xu, Z., 2004, Timing of granite emplacement and cooling in the Songpan-Garzê Fold Belt (eastern Tibetan Plateau) with tectonic implications: Journal of Asian Earth Sciences, v. 22, p. 465–481, doi: 10.1016/S1367-9120(03)00089-0.

Royden, L.H., Burchfiel, B.C., King, R.W., Wang, E., Chen, Z., Shen, F., and Liu, Y., 1997, Surface deformation and lower crustal flow in eastern Tibet: Science, v. 276, p. 788–790, doi: 10.1126/science.276.5313.788.

Schoenbohm, L.M., Whipple, K.X., Burchfiel, B.C., and Chen, L., 2004, Geomorphic constraints on surface uplift, exhumation, and plateau growth in the Red River region, Yunnan Province, China: Geological Society of America Bulletin, v. 116, p. 895–909.

Schwab, M., Ratschbacher, L., Siebel, W., McWilliams, M.O., Lutkov, V., Minaev, V., Chen, F., Stanek, K.-P., Nelson, B., Frisch, W., and Wooden, J., 2004, Assemblage of the Pamirs: Age and origin of magmatic belts from the southern Tien Shan to the southern Pamirs and their relation to Tibet: Tectonics, v. 23, p. TC4002, p. 1–31, doi: 10.1029/2003TC001583.

Spang, J.H., 1972, Numerical method for dynamic analysis of calcite twin lamellae: Geological Society of America Bulletin, v. 83, p. 467–472.

Sperner, B., Ratschbacher, L., and Ott, R., 1993, Fault-striae analysis: a TURBO PASCAL program package for graphical presentation and reduced stress tensor calculation: Computers & Geosciences, v. 19, p. 1361–1388, doi: 10.1016/0098-3004(93)90035-4.

Tapponnier, P., and Molnar, P., 1977, Active faulting and tectonics in China: Journal of Geophysical Research, v. 82, p. 2905–2930.

Tapponnier, P., Xu, Z., Roger, F., Meyer, B., Arnaud, N., Wittlinger, G., and Yang, J., 2001, Oblique stepwise rise and growth of the Tibet Plateau: Science, v. 294, p. 1671–1677, doi: 10.1126/science.105978.

Turner, F.J., 1953, Nature and dynamic interpretation of deformation lamellae in calcite of three marbles: American Journal of Science, v. 251, p. 276–298.

Van den haute, P., Jonckheere, R., and De Corte, F., 1988, Thermal neutron fluence determination for fission-track dating with metal activation monitors: A re-investigation: Chemical Geology, v. 73, p. 233–244.

Wagner, G.A., 1988, Apatite fission-track geochronothermometer to 60°C: Projected length studies: Chemical Geology, v. 72, p. 145–153.

Wagner, G.A., Gleadow, A.J.W., and Fitzgerald, P.G., 1989, The significance of the partial annealing zone in apatite fission track analysis: Projected track length measurements and uplift chronology of the Transantarctic Mountains: Chemical Geology, v. 79, p. 295–305.

Wang, E., and Burchfiel, B.C., 2000, Late Cenozoic to Holocene deformation in southwestern Sichuan and adjacent Yunnan, China, and its role in formation of the southeastern part of the Tibetan Plateau: Geological Society of America Bulletin, v. 112, p. 413–423, doi: 10.1130/0016-7606(2000)112<0413:LCTHDI>2.3.CO;2.

Watt, S., and Durrani, S.A., 1985, Thermal stability of fission tracks in apatite and sphene: Using confined track length measurements: Nuclear Tracks, v. 10, p. 349–357.

Watt, S., Green, P.F., and Durrani, S.A., 1984, Studies of annealing anisotropy of fission tracks in mineral apatite using track-in-track (TINT) length measurements: Nuclear Tracks, v. 8, p. 371–375.

Webb, L.E., Hacker, B.R., Ratschbacher, L., McWilliams, M.O., and Dong, S., 1999, Thermochronologic constraints on deformation and cooling history of high- and ultrahigh-pressure rocks in the Qinling-Dabie orogen, eastern China: Tectonics, v. 18, p. 621–637, doi: 10.1029/1999TC900012.

Webb, L.E., Ratschbacher, L., Hacker, B.R., and Dong, S., 2001, Kinematics of exhumation of high- and ultrahigh-pressure rocks in the Hong'an and Tongbai Shan of the Qinling-Dabie collisional orogen, eastern China: Geological Society of America Memoir 194, p. 231–245.

Wessel, P., and Smith, H.F., 1995, New version of the Generic Mapping Tools released: Eos (Transactions of the American Geophysical Union), v. 76, p. 329.

Wilson, C.J.L., Harrowfield, M.J., and Reid, A.J., 2005, Brittle modification of Triassic architecture in eastern Tibet: Implications for the construction of the Cenozoic plateau: Journal of Asian Earth Sciences, doi:10.1016/j.jseaes.2005.04.004.

Xu, G., and Kamp, P.J.J., 2000, Tectonics and denudation adjacent to the Xianshuihe Fault, eastern Tibetan Plateau; constraints from fission track thermochronology: Journal of Geophysical Research, v. 105, p. 19,231–19,251, doi: 10.1029/2000JB900159.

Zhang, P.-Z., Shen, Z., Wang, M., Gan, W., Bürgmann, R., Molnar, P., Wang, Q., Niu, Z., Sun, J., Wu, J., Hanrong, S., and Xinzhao, Y., 2004, Continuous deformation of the Tibetan Plateau from global positioning system data: Geology, v. 32, p. 809–812.

Zhang, Y.Q., Vergely, P., and Mercier, J., 1995, Active faulting in and along the Qingling Range (China) inferred from SPOT imagery analysis and extrusion tectonics of south China: Tectonophysics, v. 243, p. 69–95, doi: 10.1016/0040-1951(94)00192-C.

Zhang, Y.Q., Mercier, J.L., and Vergely, P., 1998, Extension in the graben system around the Ordos (China), and its contribution to the tectonics of south China with respect to Gobi-Mongolia: Tectonophysics, v. 285, p. 41–75, doi: 10.1016/S0040-1951(97)00170-4.

Zhang, Y., Dong, S., and Shi, W., 2003, Cretaceous deformation history of the middle Tan-Lu fault zone in the Shandong Province, eastern China: Tectonophysics, v. 363, p. 243–258, doi: 10.1016/S0040-1951(03)00039-8.

Zhao, W., Mechie, J., Brown, L.D., Guo, J., Haines, S., Hearn, T., Klemperer, S.L., Ma, Y.S., Meissner, R., Nelson, K.D., Ni, J.F., Pananon, P., Rapine, R., Ross, A., and Saul, J., 2001, Crustal structure of central Tibet as derived from project INDEPTH wide-angle seismic data: Geophysical Journal International, v. 145, p. 486–498, doi: 10.1046/j.0956-540x.2001.01402.x.

Manuscript Received by the Society 9 February 2005
Revised Manuscript Received 3 January 2006
Manuscript Accepted 5 February 2006

Printed in the USA